Neutron Stars and NuSTAR

A Systematic Survey of Neutron Star Masses in High Mass X-ray Binaries

&

Characterization of CdZnTe Detectors for NuSTAR

A Thesis by
Varun B. Bhalerao
Advisors
Professors Fiona Harrison & Shri R. Kulkarni

In Partial Fulfillment of the Requirements
for the Degree of
Doctor of Philosophy

California Institute of Technology
Pasadena, California

2012

(Defended May 24, 2012)

Dedicated to my parents,
Erawati and Bhalchandra Bhalerao
my role models, motivation,
and strength.

Acknowledgments

My six years at Caltech have been an amazing experience, in both work and personal life. As I write this thesis summarizing the work, it is fitting that I begin by thanking the many people who have made my little achievement possible.

I am very fortunate to have Professors Fiona Harrison and Shri Kulkarni as my advisors. Their foresight, work ethic, and complementary styles of mentoring provided all the ingredients necessary to take me through my thesis. They have provided all resources I needed, and key insights whenever I was short on ideas (or had too many). I have learned a lot from working with them, and will continue striving to live up to their standards.

Working on NuSTAR has been a dream come true. No, really. Who has not wanted to build and launch a satellite? My work would have been impossible without significant help from my lab partners Brian Grefenstette and Vikram Rana. As the junior-most member in the Caltech NuSTAR team, I was the least experienced. I am grateful to Eric Bellm, Jill Burnham, Rick Cook, Takao Kitaguchi, Kristin Madsen, Peter Mao, and Hiromasa Miyasaka for helping me whenever I was stuck. I thank Peter's dentist. Miles Robinson, Steve Stryker, and Robert Crabill have been wonderful troubleshooters and the go-to people for any work in the laboratory. Summer projects by students Nancy Wu and Suk Sien Tie laid good foundations for my future work.

As an electrical engineer, I had a lot to learn about astronomy. My foray into observations was possible thanks to the enthusiastic guidance of Mansi Kasliwal. I thank Professor Marten van Kerkwijk for teaching me how to extract every last bit of information from data—a skill I still strive to perfect. Brad Cenko was extremely helpful in my first year photometer project. I thank Mike Muno for his early work on radial velocities of high mass X-ray binaries, which developed into my observational project. My batchmates Laura, Walter, Matthew, and Yacine have been a constant source of support and inspiration at

Caltech. My work would have been nowhere as much fun without my long-time officemates Gwen and Laura. Together with Mansi, Shriharsh, Swarnima, and Abhilash, they made work a lot of fun! Shriharsh was the sounding board for new ideas at work. I am glad to have the company of Swarnima, Ryan and Krzysztof to share my passion of outreach and amateur astronomy.

Part of what makes Caltech special is the excellent administrative and technical staff, whose success lies in the fact that they are always in the background. My first-year project and subsequent observing runs and Palomar were a pleasure thanks to Kevin Rykoski, Dipali, and Jean Mueller. I thank Richard Dekany, Dan McKenna, and Jeff Zolkower for support on my first year project. The ADPF group, especially Partrick Shopbell and Anu Mahabal, have maintained an excellent computing infrastructure—giving me freedom from install logs and core dumps. Librarians Lindsay Cleary and Joy Painter always went out of their way to help with procuring and issuing books. Special thanks to the several administrative assistants at Caltech: Debby Miles, Nina Borg, and Caprece Anderson at the Space Radiation Laboratory, Bronagh Glaser at Geology and Planetary Sciences, Gina Armas and Gita Patel in Robinson and Cahill, and Teresita Legaspi at the Registrar's Office. Their untiring efforts ensured that I could focus on my work without ever being bogged down by paperwork.

The reason I can put my work at the forefront is an extremely supportive family. None of this would have been possible without the effort and encouragement of my parents, who have placed me and my career ahead of everything else. Sneha has been my motivation through this final phase of my Ph.D.. My extended family, Shri and Shaila Mate, Prasanna, Madhuri, and Amruta Mate have always been around for me. Games with the badminton group at Caltech were a constant source of refreshment (and exercise!). And finally, my family away from home: Mansi, Prabha, Pinkesh, Jayakrishnan, Sushree, Shriharsh, and Ishwari, who have done everything possible to keep me happy. Thank you. *You're awesome*!

Abstract

My thesis centers around the study of neutron stars, especially those in massive binary systems. To this end, it has two distinct components: the observational study of neutron stars in massive binaries with a goal of measuring neutron star masses and participation in NuSTAR, the first imaging hard X-ray mission, one that is extremely well suited to the study of massive binaries and compact objects in our Galaxy.

The Nuclear Spectroscopic Telescope Array (NuSTAR) is a NASA Small Explorer mission that will carry the first focusing high energy X-ray telescope to orbit. NuSTAR has an order-of-magnitude better angular resolution and has two orders of magnitude higher sensitivity than any currently orbiting hard X-ray telescope. I worked to develop, calibrate, and test `CdZnTe` detectors for NuSTAR. I describe the `CdZnTe` detectors in comprehensive detail here—from readout procedures to data analysis. Detailed calibration of detectors is necessary for analyzing astrophysical source data obtained by the NuSTAR. I discuss the design and implementation of an automated setup for calibrating flight detectors, followed by calibration procedures and results.

Neutron stars are an excellent probe of fundamental physics. The maximum mass of a neutron star can put stringent constraints on the equation of state of matter at extreme pressures and densities. From an astrophysical perspective, there are several open questions in our understanding of neutron stars. What are the birth masses of neutron stars? How do they change in binary evolution? Are there multiple mechanisms for the formation of neutron stars? Measuring masses of neutron stars helps answer these questions. Neutron stars in high-mass X-ray binaries have masses close to their birth mass, providing an opportunity to disentangle the role of "nature" and "nurture" in the observed mass distributions. In 2006, masses had been measured for only six such objects, but this small sample showed the greatest diversity in masses among all classes of neutron star binaries. Intrigued by

this diversity—which points to diverse birth masses—we undertook a systematic survey to measure the masses of neutron stars in nine high-mass X-ray binaries. In this thesis, I present results from this ongoing project.

While neutron stars formed the primary focus of my work, I also explored other topics in compact objects. appendix A describes the discovery and complete characterization of a 1RXS J173006.4+033813, a polar cataclysmic variable. appendix B describes the discovery of a diamond planet orbiting a millisecond pulsar, and our search for its optical counterpart.

Contents

List of Figures

List of Tables

List of Acronyms

ADC: analog-to-digital convertor

AGN: active galactic nuclei

ASIC: application-specific integrated circuit

BH: black hole

cps: counts per second

DBSP: double beam spectrograph

EOS: equation of state

ESD: electrostatic discharge

FITS: flexible image transport system

FOV: field of view

FPGA: field programmable gate array

FPM: focal plane module

FWHM: Full Width at Half Maximum

GUI: graphical user interface

HEASARC: high energy astrophysics science archive research center

HMXB: high-mass X-ray binary

HPD: half power diameter

HV: high voltage

IC: integrated circuit

IR: infrared

LRIS: low resolution imaging spectrograph

MISC: minimum instruction set computer

MOC: mission operations center

NRL: naval research laboratory

NS: neutron star

NuSTAR nuclear spectroscopic telescope array

NuSTARDAS: NuSTAR data analysis software

OGIP: office of guest investigator programs

PH: pulse height

PI: pulse invariant

PMT: photomultiplier tube

PSF: point-spread function

RMF: redistribution matrix file

QE: quantum efficiency

RV: radial velocity

SAA: south atlantic anamoly

SFXT: supergiant fast X-ray transient

SMBH: super massive black hole

SMEX: small explorer

SNR: signal-to-noise ratio

SOC: science operations center

SRL: space radiation laboratory

ToO: target of opportunity

XRB: X-ray binary

Part One: NuSTAR

Characterization of CdZnTe Detectors for NuSTAR

Image: NuSTAR satellite at Orbital Sciences Corporation

NuSTAR

Part Two: Masses of Neutron Stars

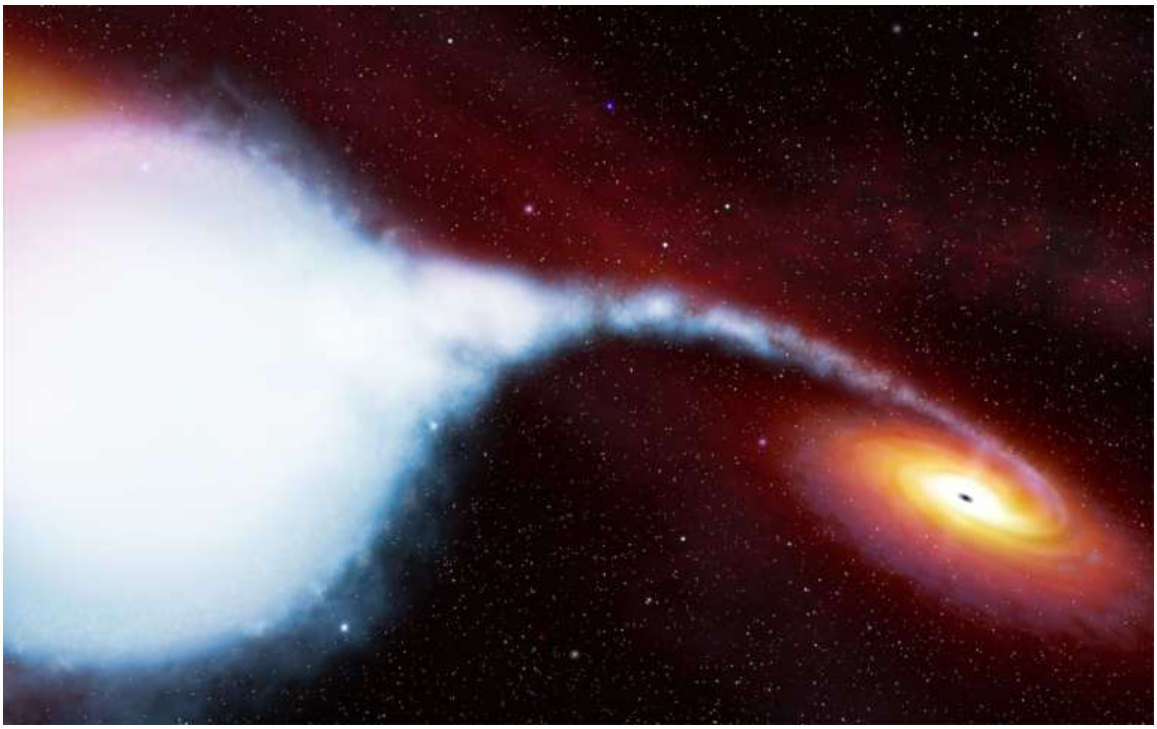

X-Mas: A Search for eXtra Massive Neutron Stars

Image: Artists illustration of a galactic Black Hole high-mass X-ray binary Cygnus X-1.

Credit: ESA/Hubble, via Wikimedia Commons.

Chapter 4

High-Mass X-ray Binaries

This part of the thesis focuses on the masses of neutron stars. In this Chapter, I motivate the case for measuring neutron star masses. Then I narrow down the sample to high-mass X-ray binaries and discuss the methods and techniques for measuring masses. In Chapters 5 and 6, I provide the results of X-Mas: our systematic survey of neutron star masses in high-mass X-ray binaries to shed light on the formation processes of NSs. In Chapter 7, I describe some constraints on the evolution of a two solar mass neutron star.

4.1 Weighing in on Neutron Stars

Neutron stars (NSs) are compact remnants of high mass stars. The following three questions are central to our study of neutron stars: (1) What is the relation between the mass of the progenitor star and the mass of the neutron star (the initial-final mass mapping)? (2) Are there multiple channels to form neutron stars? (3) Are there exotic states of matter in the interiors of neutron stars? As explained below, measuring the masses of neutron stars helps answer these three questions.

The global structure of a neutron star depends on the equation of state (EOS) of matter under extreme conditions, i.e., the relation between pressure and density in the neutron star. Given an EOS, the maximum mass of a neutron star can be calculated (Figure 4.1). If the EOS is "Soft," then kaon condensates or strange matter can form in the interior of neutron stars, and an upper limit of <1.55 $M_{\odot}$ is expected for NS masses (Lattimer & Prakash, 2005). Our current understanding of nuclear physics predicts a "stiff" EOS, where a given density can support higher pressure. This claim is further bolstered by the discovery of a

2 $M_\odot$ NS (Demorest et al., 2010; Lattimer et al., 2010).

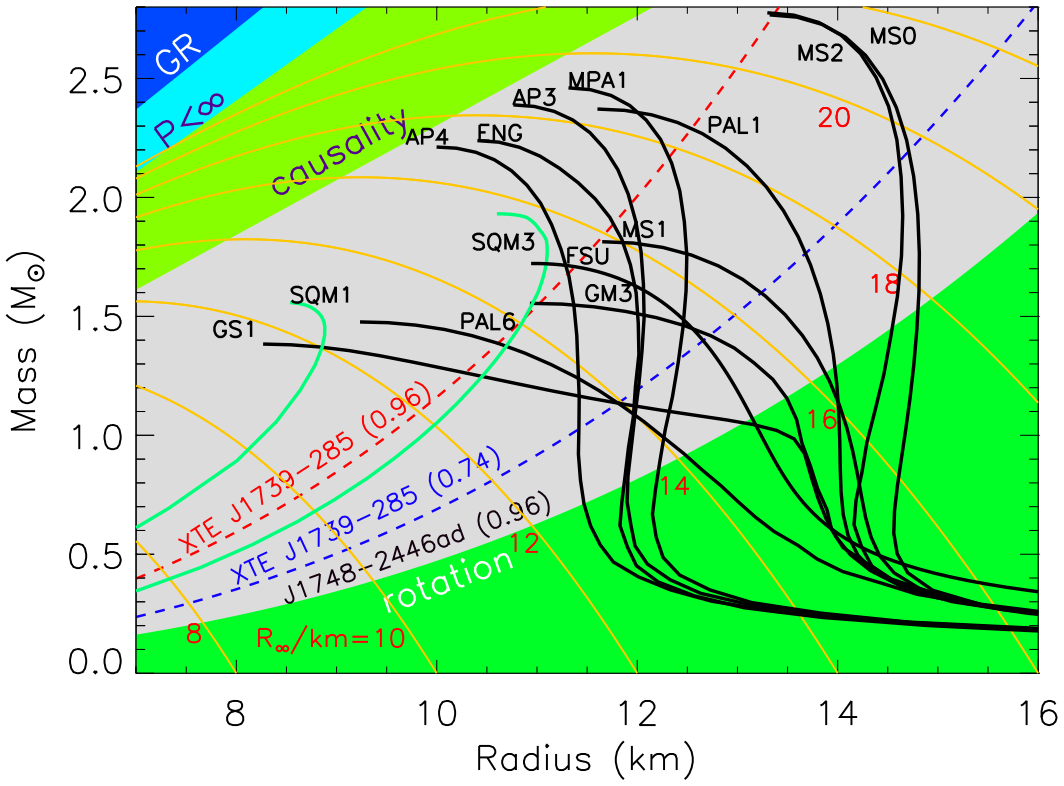

Figure 4.1. Theoretical mass-radius relationships for neutron stars. Solid curves are models calculated assuming different equations of state (EOS), labeled as per Lattimer & Prakash (2007). The discovery of massive neutron stars, e.g., the 2 $M_\odot$ PSR J1614-2230, rules out the soft equations of state. Figure credit (Lattimer & Prakash, 2007), reproduced with permission from Elsevier.

The primary observables of neutron stars—spin periods, radii, and masses—can be used to constrain their properties and internal structure. The fastest pulsar periods and periods of quasi-periodic oscillations in accreting NSs provide limits on the radii and masses of neutron stars (Lattimer & Prakash, 2007). Radii inferred from neutron star cooling or modeling of photospheric expansion bursts have also been used to test NS models from various equations of state (Steiner et al., 2010). Dynamical measurements of masses of NS in binaries provide an important test to these models. In compact object binaries (NS–NS, NS–white dwarf), very precise mass measurements can be obtained from relativistic

effects like the advance of periastron (Freire et al., 2008) or measurement of the Shapiro delay (Demorest et al., 2010).

The mass of the supernova remnant depends on the evolutionary state of the progenitor, the nature of core collapse (CC), and post-CC evolution. I restrict the discussion here to birth masses of neutron stars, and revisit some aspects of post-CC evolution in our work on the companion to the 2 $M_\odot$ PSR J1614-2230 in Chapter 7. Model calculations by Timmes et al. (1996) predict that type II (core-collapse) supernovae should form NSs with a bimodal distribution of masses peaked at 1.28 and 1.73 $M_\odot$, while Ib supernovae will produce NSs with masses in a small range around 1.32 $M_\odot$. If the NS is born in a binary, then it may accrete matter from the companion, spreading out these distributions. In addition, neutron stars formed in electron-capture supernovae likely have lower mass (Nomoto, 1984), and may be present in some of the binary pulsars (Schwab et al., 2010). Knigge et al. (2011) suggested that this alternative formation channel might also account for the observed bimodality in the properties of Be X-ray binaries, where in contrast to the majority of systems, some have low eccentricity, suggesting a small natal kick.

As of summer 2012, masses have been measured for over fifty five neutron stars. The dynamical masses of neutron stars can be measured only in binary systems. Most of the mass measurements are for NSs in radio pulsar binaries or NS-white dwarf (WD) binaries. Several groups have analyzed the mass measurements and inferred that NS masses have a bimodal distribution (Kiziltan et al., 2010; Zhang et al., 2011; Valentim et al., 2011; Özel et al., 2012). This bimodality likely stems from NSs accreting mass from their companion during the spin-up (recycling) process. The differences in mass accreted in the recycling process may dominate over any intrinsic variations in the birth masses of such pulsars. Being restricted to these two types of binaries may not reveal the complete range of neutron star masses.

The third major class of NS binaries, X-ray binaries (XRBs), trace distinct evolutionary pathways for NSs. XRBs are sub-divided into high-mass X-ray binaries (HMXBs) and low mass X-ray binaries (LMXBs) based on the spectral type and mass of the companion star. My work focuses on the HMXB subset of this population, which we explore in detail next.

[1] A complete list of measured masses is at http://stellarcollapse.org/nsmasses.

4.2 High-Mass X-ray Binaries

High mass X-ray binaries (HMXBs) are binary systems containing a neutron star or a black hole (secondary) and massive ($\gtrsim$ 8 $M_\odot$) OB (primary) companions, with orbital periods ranging from days to months. In 2006, there were 114 known HMXBs in the Milky Way (Liu et al., 2006) and 128 in the Magellanic Clouds (Liu et al., 2005). A new population of highly obscured HMXBs was discovered by the *Integral* satellite (Chaty et al., 2010). In this thesis, I discuss HMXBs with a NS as the secondary, unless explicitly stated otherwise.

High mass X-ray binaries can be observationally divided into several types:

1. *Be X-ray binaries* have a non-supergiant, fast-rotating Be star as the optical companion (e.g., Cep X-4, GX 304 − 1). Compared to normal B-type stars, Be stars show emission lines and excess infrared emission at some point in their lives. These features are attributed to the formation of an equatorial disc around the star, the origins of which are not fully understood yet (Reig, 2011, and references therein). Most Be XRBs have eccentric orbits ($e \gtrsim 0.3$) and show transient X-ray emission near periastron passages, though lower luminosity persistent systems also exist. Almost all Be XRBs show X-ray pulsations and are inferred to have NS counterparts: there are no candidate Be–black hole binaries (Paul & Naik, 2011; Reig, 2011).

2. *Classical X-ray binaries* are XRBs where the optical companion is a supergiant OB star (Chaty, 2011). This companion emits a substantial wind, and the NS orbits inside this wind (e.g., Vela X-1). Although capture from a high-velocity stellar wind is inefficient, the large mass-loss rate in the wind can result in an appreciable mass accretion rate onto the neutron star that is sufficient to emit radiation in X-ray band (Paul & Naik, 2011). In some objects of this type, the orbit is compact enough that the OB star fills its Roche lobe. For such objects, the accretion rate is greatly enhanced and may be mediated through an accretion disc (e.g., SMC X-1, LMC X-4).

3. *Supergiant Fast X-ray Transients (SFXTs)* are hard X-ray transients with a high dynamic range (10 − 10) in their X-ray lightcurves (e.g., IGR J17544−2619, AX J1841.0−0536). They show recurrent outbursts on few-hour timescales, superposed on outbursts lasting a few days (Sidoli, 2011). This is a relatively new class with about 10 members, all of which are associated with blue supergiants. Pulsations

have been detected in only five of the SFXTs (Sidoli, 2011), but it is generally assumed that all SFXTs harbor neutron stars. This class is sometimes considered a subclass of classical HMXBs and it is possible that SFXTs and classical wind-fed HMXBs lie along a continuum (Chaty, 2011).

NS masses in HMXBs will be close to the birth masses. After the neutron star is formed, it can accrete mass from the companion by various mechanisms like wind accretion, disk accretion, or Roche lobe overflow. If the accretion is spherically symmetric, it will be limited by the Eddington accretion rate. For a NS of radius $\sim$ 14 km, the limiting accretion rate is $\dot{M}$ $\approx 2 \times 10^{-}$ $M_{\odot}$ yr^{-} , independent of its mass. In this case, in the $\sim$10 yr lifetime of the OB companion, the NS can accrete at most $\sim$0.1 $M_{\odot}$. Hence, measuring the masses of NSs in HMXBs allows us to measure the distribution of their birth masses.

Radial velocity measurements for these OB stars are complicated by several factors. Some of the spectral lines, especially Hα and Hβ, are variable. In some objects, lines are produced at different parts of the stellar photosphere and may have different radial velocities. Many of the systems are highly extincted and are visible only in IR. However, among the very few measurements, there is a large scatter in masses (Table 4.1). Among the five HMXBs with reasonably secure masses, one has a high value of $M = 1.8 \pm 0.3$ $M_{\odot}$ (Vela X$-$1; Barziv et al., 2001; Quaintrell et al., 2003). As discussed above this indicates that this neutron star may have been born heavy.

4.3 NS mass measurements in HMXBs

Motivated by the spread in known NS masses in HMXBs despite them being close to their masses at birth, we undertook "X-Mas," an extensive program to measure masses for more such neutron stars by radial velocity (RV) studies of the OB companions. Here I outline the general method, observations and data analysis for such mass measurements. In Chapter 5, I present first results for a few HMXBs obtained from data taken with the 200" Hale telescope at Palomar, followed by the constraints on the mass of the compact object in an eclipsing HMXB in M33 (Chapter 6).

Table 4.1. Masses of neutron stars in high-mass X-ray binaries

Object	M	M	Reference
4U1700-37	2.44±0.27	58±11	Clark et al. (2002)
4U1538-52	1.06^{+}_{-}	···	van Kerkwijk et al. (1995)
SMC X-1	1.06^{+}_{-}	15.7^{+}_{-}	van der Meer et al. (2007)
Cen X-3	1.34^{+}_{-}	20.2^{+}_{-}	van der Meer et al. (2007)
LMC X-4	1.25^{+}_{-}	14.5^{+}_{-}	van der Meer et al. (2007)
Vela X-1	1.88±0.13	23.1±0.2	Barziv et al. (2001); Quaintrell et al. (2003)
	2.27±0.17	27.9±1.3	
EXO 1722-363	1.4±0.4	13.6±1.6	Mason et al. (2010)
	1.5±0.4	15.2±1.9	
IGR J18027-2016	1.4±0.2	18.6±0.8	Mason et al. (2011b)
	1.6±0.3	21.8±2.4	
OAO 1657-415	1.4±0.3	14.2±0.4	Mason et al. (2011a)
	1.7±0.3	17.0±0.7	

Assuming edge-on orbit ($i = 90°$).

Assuming Roche lobe filling companion ($\beta = 1$).

4.3.1 Method

The masses of both components in a binary can be calculated by characterizing its orbit. A binary orbit is fully described by seven orbital elements: the semi-major axis (a), period (P), eccentricity (e), inclination (i), longitude of the ascending node (Ω), longitude of periastron (ω) and the time of periastron passage (T) (Figure 4.2). In HMXBs, the orbital elements for the NS are often calculated by X-ray pulse timing measurements in different parts the orbit. In our study, we measure the radial velocity of the OB companion around the orbit. Using the optical and X-ray data, we can calculate the mass function, and in some cases the mass of the neutron star.

We follow the method introduced by Joss & Rappaport (1984), which is widely used (see for example, van der Meer et al., 2007; Mason et al., 2011b). We can write the masses of the optical companion and the X-ray source (M and M , respectively) in terms of the mass functions:

$$M = \frac{K \; P(1-e\;)^{/}}{2\pi G \sin\; i}(1+q)\;, \tag{4.1}$$

and

$$M = \frac{K \quad P(1-e\;)^{/}}{2\pi G \sin\; i}\left(1+\frac{1}{q}\right)\;, \tag{4.2}$$

where K and K are the semiamplitudes of the respective radial velocity curves, (i) is the inclination, and q is the mass ratio of the components, defined as

$$q \equiv \frac{M}{M} = \frac{K}{K}. \tag{4.3}$$

In practice, X-ray timing results are often quoted as the projected semi-major axis of the pulsar's orbit in light-seconds, $a \sin i$, from which we get $K = 2\pi c\; a \sin i/P$. Our optical or IR spectra can provide a value for K .

[2] i is defined as the angle between the orbital plane to the line of sight, with 90° being edge-on.

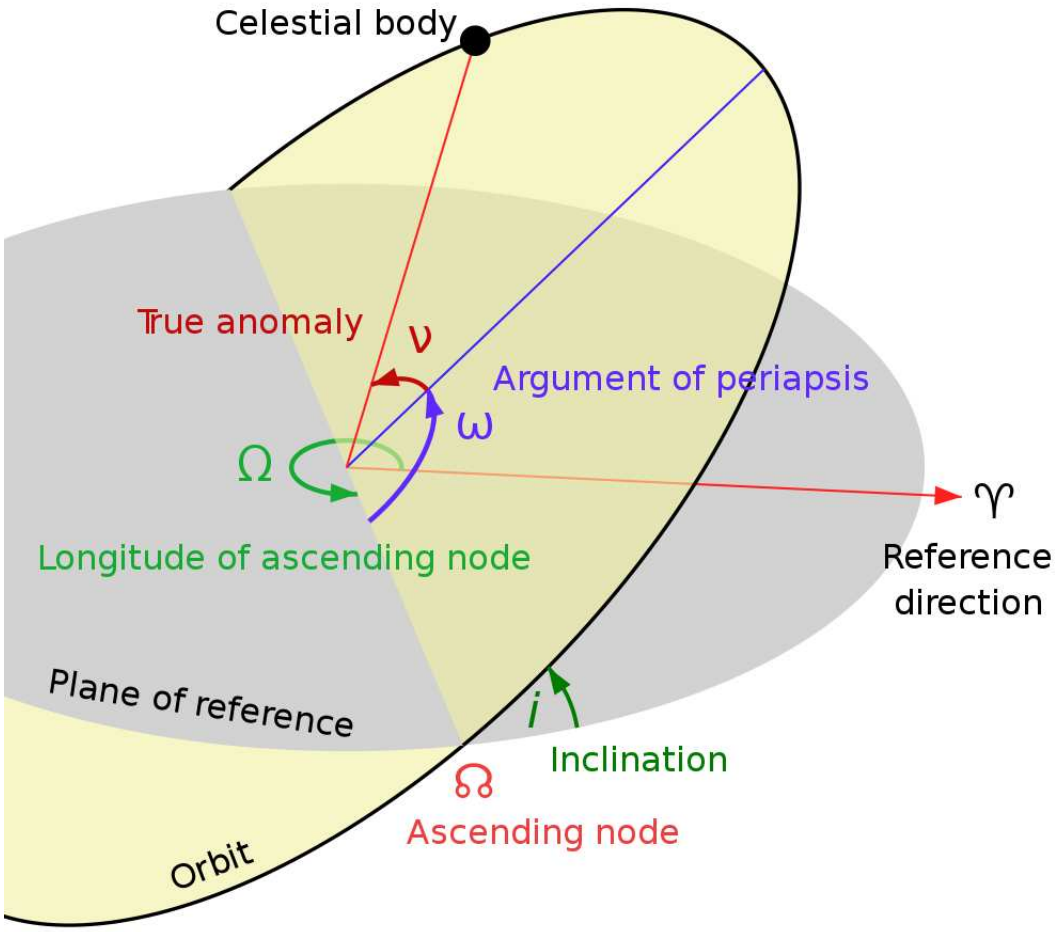

Figure 4.2. The elements of an elliptical orbit. The observer is located below the the gray horizontal plane of reference, viz., the sky plane. All angles are measured with the center of mass of the orbit as the vertex. The inclination of the orbit to the sky plane (i) is measured such that $i = 90°$ for an edge-on orbit. The ascending node is where the object crosses the plane of the sky, receding from the observer. The longitude of the ascending node (Ω) is the angle between the reference direction Υ (north) and the ascending node. It can be measured only for resolved binaries, and does not enter our calculations. The argument of periastron (ω) is the angle in the plane of the orbit between the periastron (periapsis) and the ascending node. At a given time T, the location of the object along the orbit is given by its true anomaly ν. The reference time T_0 is usually defined as the time when the object is at periastron.

Image reproduced from Wikimedia Commons (http://commons.wikimedia.org/wiki/File:Orbit1.sv

The orbital inclination is usually unknown, making it impossible to solve explicitly for component masses. Equations (4.1) and (4.2) are then recast in terms of the mass function f:

$$\begin{aligned} f &\equiv \frac{M \sin i}{(M + M)} \\ &= \frac{K P(1-e)^{/}}{2\pi G} \\ &= 1.036 \times 10^{-} (1-e)^{/} K P \, \mathrm{M}_{\odot}, \end{aligned} \tag{4.4}$$

where mass is measured in solar masses, velocity in kilometers per second and period in days.

Since $\sin i \leq 1$, we can use Equation (4.4) to calculate a lower limit M as a function of M . In turn, M can be estimated from the spectral class of the OB star. For most of the systems in our sample, we calculate such lower bounds on masses (Chapter 5).

If the HMXB shows eclipses, we can calculate the inclination from the eclipse duration. Assuming a spherical companion star, the inclination of the system is related to the eclipse half-angle θ_e, the stellar radius R, and the orbital separation a by

$$\sin i = \frac{\sqrt{1-(R/a)}}{\cos\theta_e}. \tag{4.5}$$

Following the approach in Rappaport & Joss (1983), the radius of the companion star is some fraction of the effective Roche lobe radius,

$$R = \beta R_L, \tag{4.6}$$

where R_L is the sphere-equivalent Roche lobe radius. We will refer to the fraction β as the "Roche lobe filling factor." Combining Equations (4.5) and (4.6) yields

$$\sin i = \frac{\sqrt{1-\beta (R_L/a)}}{\cos\theta_e}. \tag{4.7}$$

For a co-rotating secondary, Eggleton (1983) gives an expression for R_L/a, the ratio of

[3]The eclipse half-angle θ_e, or more specifically the semi-eclipse angle of the neutron star, represents half of the eclipse duration.

the effective Roche lobe radius and the orbital separation:

$$\frac{R_L}{a} \approx \frac{0.49q^{-/}}{0.6q^{-/} + \ln(1+q^{-/})}. \tag{4.8}$$

In some cases, the secondary star might not be corotating with the system. The ratio of the rotational frequency of the optical companion to the orbital frequency of the system is defined as Ω. In other words, it is a measure of the degree of synchronous rotation, where $\Omega = 1$ is defined to be synchronous. In this case, we use approximations by Rappaport & Joss (1983):

$$\frac{R_L}{a} \approx A + B\log q + C\log q, \tag{4.9}$$

where the constants A, B, and C are

$$\begin{aligned} A &= 0.398 - 0.026\Omega + 0.004\Omega, \\ B &= -0.264 + 0.052\Omega - 0.015\Omega, \\ C &= -0.023 - 0.005\Omega. \end{aligned} \tag{4.10}$$

These four expressions give the value of R_L to an accuracy of about 2% over the ranges of $0 \leq \Omega \leq 2$ and $0.02 \leq q \leq 1$ (Joss & Rappaport, 1984). If we substitute $\Omega = 1$ in Equation (4.10), then the R_L/a values of Equations (4.8) and (4.9) agree to within 1% in the range $0.01 \lesssim q \lesssim 1$.

In noneclipsing binaries, $\sin i$ is usually unconstrained. For such binaries, we can only place lower limits on M (Equation (4.4)). In binaries without accurate NS pulse timing data, neither K nor $a \sin i$ are known. For such systems, the mass estimates are indirect. Where good spectra are available, they can be used to estimate the spectral type and thereby the mass of the optical component. In rare cases where the distance to the binary is known, it provides an independent constraint on the physical scale of the system—for example by calculating the absolute magnitude of the components (Chapter 6). However, calculating masses from these methods is model dependent to some extent.

4.3.2 Observations

The accurate measurement of radial velocities, and in turn of orbital solutions, depends on several factors before, during and after the observing run. This chapter provides a general overview of the observing procedure, more details of specific observing runs are given in Chapters 5 and 6.

For our program, the key factors for an observing run are

1. Select proper instrument settings to cover all prominent spectral features with sufficient wavelength resolution,

2. Calculate the desired SNR and deduce the exposure time,

3. Select epochs of observation to maximize phase coverage,

Depending on the spectral and luminosity class, OB star spectra have strong Balmer series lines, as well as lines from He, C, N, O etc. in the blue part of the optical spectrum (∼3500 Å–5500 Å). In contrast, there are considerably fewer spectral features at wavelengths longer than ∼5500 Å. The SNR of the spectra at these wavelengths is lower, as the flux of OB stars in this wavelength range is lower than the blue range, and the background noise is higher due to intrinsic sky emission. Hence, we concentrate on the blue spectra for measuring radial velocities. The absorption lines are rotationally broadened to few hundred kilometers per second, corresponding to a FWHM of few angstroms in this wavelength range. Thus, low resolution spectrographs with resolving power of few thousand are sufficient to resolve the lines. Considering the large desired wavelength coverage, we selected the Double Beam Spectrograph on the 5 m Hale telescope at Palomar (DBSP; Oke & Gunn, 1982) for most of our observations. For the fainter target XMMU J013236.7+303228 (Chapter 6), we obtained data with the Low Resolution Imaging Spectrograph on the 10 m Keck-I telescope (LRIS; Oke et al., 1995), with upgraded blue (McCarthy et al., 1998; Steidel et al., 2004) and red cameras (Rockosi et al., 2010).

We planned exposures to ensure all acquired spectra have a high enough signal-to-noise ratio for measuring radial velocities with desired accuracy, as follows: From Equation (4.1), the mass depends on K . To measure M with ∼10% accuracy, we need to measure K with ∼3% accuracy. Typical values of K for HMXBs are few tens of kilometers per second,

and we had planned a few epochs per target, so this translates to a requirement of measuring velocity with an accuracy of about 5 km s^{-} per epoch. I simulated DBSP and LRIS spectra and measured radial velocities from them to calculate expected errors as a function of SNR. Our project requires SNR of ∼100 per pixel, which translates to an exposure time of 80 min for a $m_V = 15$ target with DBSP. In practice, we divided this exposure time into four or more spectra, measured velocities on each spectrum independently, and combined the results into a single velocity measurement for that epoch.

To fit an orbit to radial velocity data, measurements need to be well spaced in orbital phase. Ideally, monitoring programs like RV measurements are best executed on queue–scheduled telescopes. For our program at Palomar, we applied for well-spaced nights. We obtained good phase coverage for most of our targets from pseudorandom spacing of these observations. Our target for the Keck observing run (XMMU J013236.7+303228) has a period of 1.73 days, so we obtained observations on two full consecutive nights. Unfortunately, the phase coverage was not optimized.

Last, but not the least, we ensured careful logging of our observing runs. Any anomalies like cloud cover, worsened seeing, tracking issues, etc., can distort the spectrum. Some of these effects can be canceled out in data analysis, while others cannot. While analyzing data, we reject some spectra based on observing logs before calculating the final orbit (see, for example, Chapter 6). In this regard, the equatorial mounting of the 200" Hale telescope is a great advantage, as it gives excellent tracking performance even at high airmass (low altitude).

4.3.3 Data Reduction and Analysis

After the observing runs, RV measurements can broadly be broken into two steps. The first step, data reduction, refers to converting the raw telescope data into spectra: a table of flux as a function of wavelength. The second step, analysis, involves calculating stellar parameters, radial velocities and binary orbits from the reduced spectra.

I used `IRAF` [4] to reduce all spectra. I trim and bias-subtract all spectra, followed by a spectral response correction to remove the small-scale variations in raw data. Then I use arc lamp exposures acquired at the start of the observing night to calculate the wavelength

[4] http://iraf.noao.edu/

solution and extract 1-D spectra from raw data. The standard procedure often involves using arc lamp exposures taken closest to the science exposure. However, I have verified that for both DBSP and LRIS, the wavelength solution is extremely stable modulo a constant offset. In other words, the relative spacing of various lines in the arc lamps is constant in all exposures taken at various telescope pointings through the night. Emission lines in the sky spectrum are extremely stable (Figueira et al., 2010) and provide an excellent reference for measuring and correcting for this offset. I use the O I 5577.340 Å line to calculate wavelength offsets for LRIS spectra, and the Hg 4046.564 Å, 4358.336 Å lines for DBSP spectra. Sesar et al. (2012, in prep) adopted this approach, and found that the velocity measurements using this method are accurate to ∼2.5 km s^{-} . Finally, I use the `standard` and `calibrate` procedures in `IRAF` to remove large-scale variations and flux calibrate the spectra.

I have developed a software (`getvel`) in `IDL` to analyze these fluxed spectra and measure radial velocities. One approach to measuring radial velocity from a spectrum is to measure the location of individual spectral lines, and to average that information (van der Meer et al., 2007). However, we often see that lines like Si IV, C III that show up in combined spectra are too weak to be detected in individual spectra. In order to utilize this information buried in noise, we measure radial velocities by fitting the entire spectrum with a template. I first determine the spectral type of the target by comparing the lines with the Gray spectral atlas [5] and those referred to in Walborn & Fitzpatrick (1990). Then I select a close range of model stellar spectra (templates) from the GAIA spectral library by Munari et al. (2005). For each observed spectrum, I measure the seeing using the width of the spectral trace in the slit direction. Then I generate an instrument response function by taking a Gaussian matched to the seeing, truncating it at the slit size, and convolving it with the pixel size. I convolve the fluxed templates this instrument response, then redshift them to a test velocity. If the extinction is known, I redden the spectrum using coefficients from Cox (2000). I use `IDL mpfit` (Markwardt, 2009) to calculate the normalization to match this spectrum with the observed spectrum, and measure the χ . By minimizing the χ over test velocities, I find the best-fit velocity and the error bars. Lastly, I convert this velocity to a barycentric radial velocity using the `baryvel` routine in Astrolib (Landsman, 1993).

[5] http://ned.ipac.caltech.edu/level5/Gray/frames.html

[6] http://www.ittvis.com/ProductServices/IDL.aspx

I use the measured radial velocities and known binary parameters like the period P, phase T , and eccentricity e to calculate the best-fit orbital solution for the secondary star. Using the orbital solution, primarily K , I calculate the mass of the neutron star following the procedures in Section 4.3.1.

Chapter 5

X-Mas at Palomar

"X-Mas" at Palomar is a systematic radial velocity survey of HMXBs using the 200" Hale telescope, with the aim of understanding the distribution of masses of NS in HMXBs. We obtained data with the Double Beam Spectrograph on six nights in 2009, hereafter referred to as "Epochs" (Table 5.1). We used the D55 dichroic to split incoming light into the blue and red channels at 5500 Å. On the blue side, we used a 1200 lines/mm grating blazed at 5000 Å, with a resolution of 0.55Å/pix. On the red side we used the 1200 lines/mm grating blazed at 7100 Å, with a resolution 0.65 Å/pix. Depending on the observing conditions, we used $1''$ or $1''.5$ wide slits. Further details of planning the observing runs and data analysis steps are detailed in Section 4.3.

We selected a total of eight NS–HMXBs with known orbital periods. The nature of the compact object can be inferred from the X-ray spectrum, as accreting black holes have harder spectra than NSs. In some objects, the presence of a NS is confirmed by detection of X-ray pulsations. Here, I present the RV measurements and analysis of six HMXBs. We obtained orbital solutions and calculate masses for two of these objects: IGR J17544-2619 (Section 5.1) and SAX J2103.5+4545 (Section 5.2). Our RV data for the Be HMXB GRO J2058+42 can used to calculate the mass if more X-ray timing data is obtained (Section 5.4). Our velocity measurements for 1H 2138+579 do not show a clear orbital trend, which is discussed in Section 5.3. We are in the process of calculating orbital solutions for two more targets: 4U 2206+543 and KS 1947+300. After we completed observations, it was discovered that two candidates were misidentified. Negueruela & Schurch (2007) had proposed a tentative counterpart for AX J1820.5−1434, however a later study by Kaur et al. (2010) confirmed another star as the optical component of this HMXB. In

case of IGR J17391-3021, the counterpart detected in IR (Smith, 2004) was misidentified in the optical band.

In this chapter I provide the early results from "X-Mas at Palomar," adding two crucial data points to the small sample of NS with known masses in HMXBs.

5.1 IGR J17544-2619

IGR J17544-2619 was discovered by *Integral* during an outburst in 2003 (Sunyaev et al., 2003). The source is a SFXT consisting of a neutron star (in 't Zand, 2005) and a supergiant O-type primary (Smith, 2004; Pellizza et al., 2006). Follow-up observations with RXTE (Rossi X-ray Timing Explorer) established the spin and orbital period of the NS: P = 71.49 s, P = 4.9278(2) d (Drave et al., 2012). However, the pulsations were seen only in one observations and could not be reproduced in our analysis of the same data. This precludes the inference of other orbital parameters, e.g., $a \sin i$.

The supergiant primary is a O9 Ia star, with $T = 31000$ K, and has foreground extinction

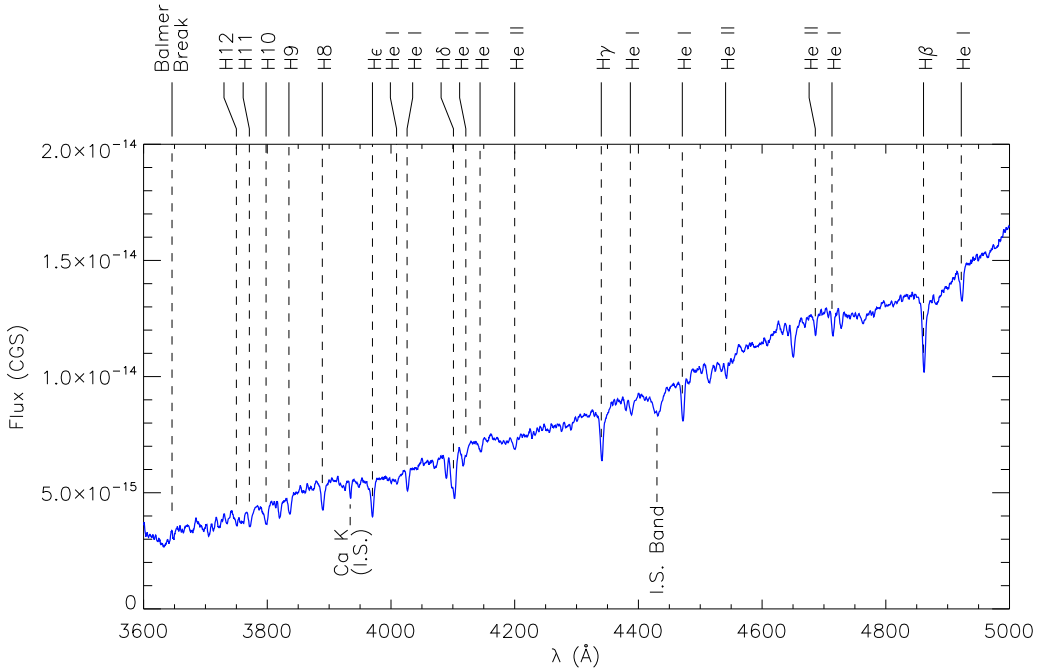

Figure 5.1. Blue side spectrum of the primary in IGR J17544-2619. Major H and He lines are marked. The primary is O9 Ia star, with $T = 31000$ K, and has foreground extinction $A_V = 6.3 \pm 0.4$ (Pellizza et al., 2006).

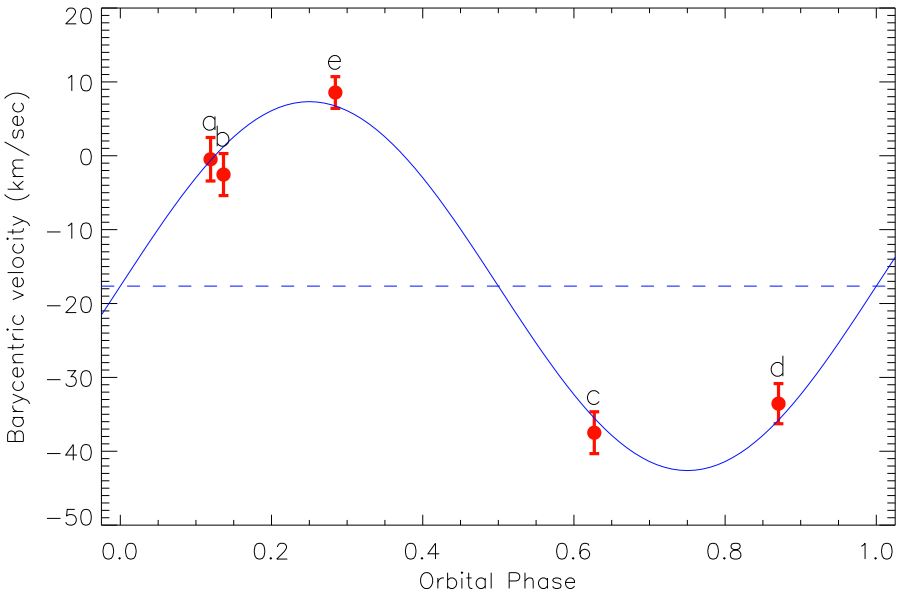

Figure 5.2. Radial velocity fit for IGR J17544-2619. We assume a circular orbit and measure $K_{\rm opt} = 25.0 \pm 1.6$ km s^{-1}, $\gamma_{\rm opt} = -17.6 \pm 1.3$ km s^{-1} and $T_0 = 2553735.77 \pm 0.07$ (HJD), with $\chi^2 = 1.8$ for two degrees of freedom.

$A_V = 6.3 \pm 0.4$ mag (Pellizza et al., 2006). We measure the temperature and extinction by fitting our spectra with model spectra with solar metallicity, no rotational broadening, and surface gravity $\log(g) = 4.0$ (Munari et al., 2005). While supergiant stars usually have $\log(g) \approx 3.0$ (Cox, 2000), our choice was governed by the availability of model spectra. Using spectra from different epochs (Figure 5.1), we infer $T = 31400 \pm 1200$ K and $A_V = 6.5 \pm 0.3$ mag, consistent with Pellizza et al. (2006) values.

We use the model atmospheres with these parameters in the `getvel` software to measure radial velocities (Table 5.1). Owing to the short orbital period and the supergiant nature of the primary, we assume that the orbit is circular. We measure K $= 25.0 \pm 1.6$ km s^{-} , γ $= -17.6 \pm 1.3$ km s^{-} and T $= 2553735.77 \pm 0.07$ (HJD), with χ $= 1.8$ for two degrees of freedom (Figure 5.2). K is robust to the choice of model atmospheres: for example, varying T from 27000 K to 33000 K changes K by less than 0.5-σ.

Pellizza et al. (2006) infer that the mass of the primary is in the range of 25 – 28 $M_\odot$. Plugging this value of K into Equation 4.4, we calculate lower limits on M as a function of M (Figure 5.3a). For M in the range 25 – 28 $M_\odot$ (Pellizza et al., 2006), the lower

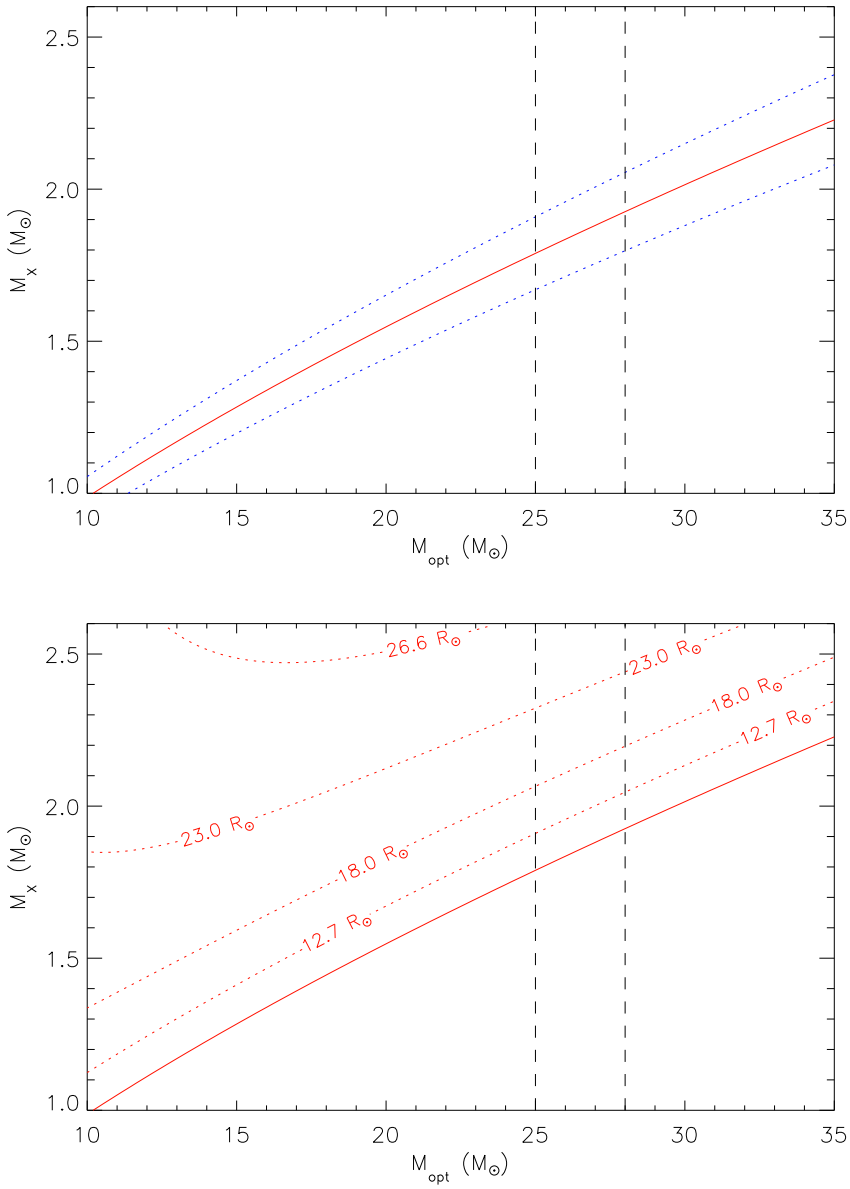

Figure 5.3. Lower limits on $M_{\rm X}$ for IGR J17544-2619. Top: The solid red curve relates $M_{\rm X}$ and $M_{\rm opt}$ assuming $\sin i = 1$, for $K_{\rm opt} = 25$ km s^{-1}. The blue curves are ± 1-σ limits corresponding to a velocity uncertainty of $\Delta K_{\rm opt} = 1.6$ km s^{-1}. The vertical black dashed lines at $M_{\rm opt}$ = 25, 28 M$_\odot$ are the bounds of $M_{\rm opt}$ from Pellizza et al. (2006). The corresponding lower limits are $M_{\rm X} > 1.79 \pm 0.11$ M$_\odot$ and $M_{\rm X} > 1.93 \pm 0.12$ M$_\odot$ respectively. Bottom: The non-detection of eclipses places upper limits on $\sin i$ as a function of the stellar radius R, changing the $M_{\rm X}$ –$M_{\rm opt}$ relation. The solid line corresponds to $\sin i = 1$ ($R = 0$), and dashed lines are contours of $M_{\rm X,min}$ for various values of R. Adopting $R_{\rm min} = 12.7$ R$_\odot$ and $M_{\rm opt,min} = 25$ M$_\odot$, we deduce $M_{\rm X} > 1.91 \pm 0.13$ M$_\odot$.

limits on the NS mass are $M > 1.79 \pm 0.12$ M$_\odot$ and $M > 1.93 \pm 0.12$ M$_\odot$ at the extreme values of M .

We further revise this estimate based on the non-eclipsing nature of this SFXT. For a circular orbit with semi-major axis a and primary stellar radius R, eclipses are seen if $\cos i < R/a$. The semi-major axis is a function of the binary period P and masses of the components. For the O star in IGR J17544-2619, 12.7 R$_\odot$ < R < 23 R$_\odot$ (Rahoui et al., 2008; Clark et al., 2009). The lower limit on R can be used to calculate a corresponding upper limit on $\sin i$. Substituting this upper limit in Equations 4.2 or 4.4, we calculate a revised lower limit on M (Figure 5.3b). For the most conservative scenario (M = 25 M$_\odot$, R = 12.7 R$_\odot$) we calculate $M > 1.91 \pm 0.13$ M$_\odot$. Using other values in the (R, M) parameter space results in even stronger lower limits (higher values of M ,).

The existence of such massive neutron stars puts strong constraints on the equation of state of matter. If X-ray pulsations are detected in IGR J17544-2619 in more epochs, we can measure $a_X \sin i$, and in turn the mass ratio q (Equation 4.3). This will provide an additional constraint on M , independent of R. Given the significant implications of verifying a high NS mass, X-ray timing observations are of utmost importance. We plan to apply for observing time with *XMM* and NuSTAR to monitor IGR J17544-2619 for pulsations.

5.2 SAX J2103.5+4545

Discovered with *BeppoSAX* in an outburst in 1997, SAX J2103.5+4545 is an an X-ray pulsar with a 358.61 s pulse period (Hulleman et al., 1998). The system is a Be HMXB, consisting of a NS and a B0 Ve star in a 12.7 d orbit. Based on the foreground extinction ($A_V = 4.2 \pm 0.3$) and spectral type, system is at 6.5 ± 0.9 kpc (Reig et al., 2004). We obtained spectra SAX J2103.5+4545 on all six "X-Mas at Palomar" epochs (Figure 5.4). Typical B0 stars have $T = 30000$ K and $\log(g) = 4.0$ (Cox, 2000). Fitting the spectra with (Munari et al., 2005) $\log(g) = 4.0$ model atmospheres as discussed in Section 5.1, we calculate $T = 29200 \pm 700$ and $A_V = 4.0 \pm 0.3$. Using spectra with $T = 30000$ K and $\log(g) = 4.0$ and varying the rotational velocity, we calculate $v \sin i = 246 \pm 8$ km s$^-$, consistent with the past measurement (240 ± 20 km s$^-$; Reig et al., 2004).

We use model stellar spectra with T=29,000 K, $\log(g)$= 4.0, and v = 250 km s$^-$ to

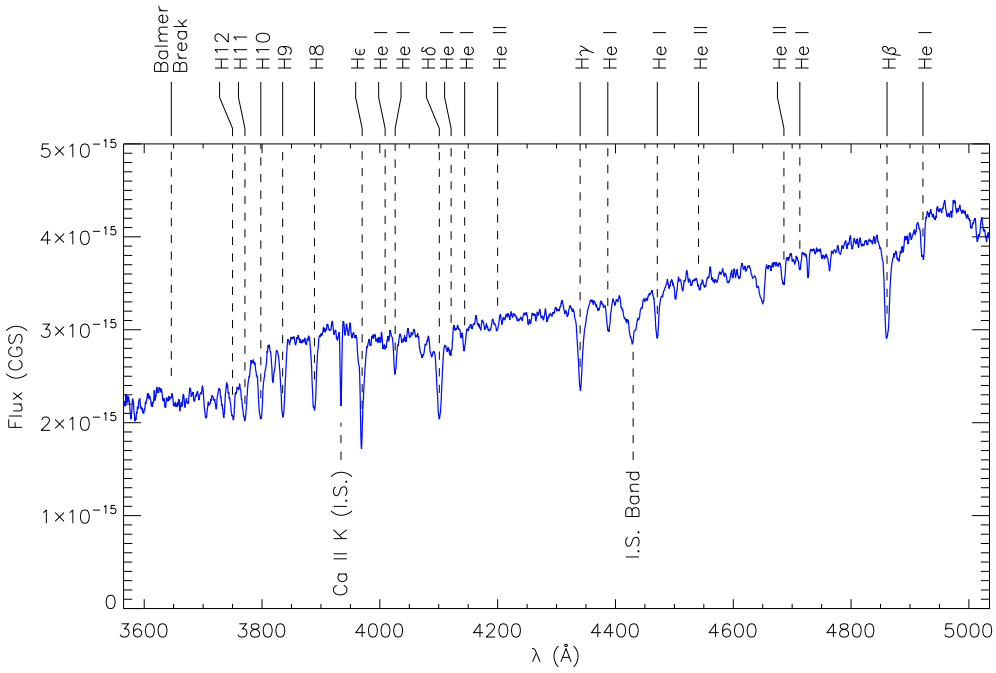

Figure 5.4. Blue side spectrum of the primary in SAX J2103.5+4545. Major H and He lines are marked. The primary is B0 Ve star, with $T = 29200 \pm 700$ K and projected rotational velocity $v_{\rm rot} \sin i = 246 \pm 8$ km s^{-1}. The broad bump in continuum around 3900 Å is an artifact of flatfielding.

calculate radial velocities (Table 5.1). Two of the four spectra acquired on 2009 Aug 23 were acquired through variable cloud cover and have low SNR. We excluded these two spectra while calculating the RV for this epoch. On folding the data at the orbital period, the data point "c" from 2009 July 31 is seen to be an outlier (Figure 5.5). Including this point in the fitting procedure does not give any satisfactory solution. We examined the observing logs and spectra to look for possible causes of a change in radial velocity, but did not find any. To verify the accuracy of our wavelength solution, we measured the centroid of the interstellar Ca K line, which should be independent of the radial velocity of the target. We found that the location of the line on this epoch is the consistent with other epochs within the $\sim$ 10 km s^{-} measurement error. We acknowledge this discrepancy but exclude this point while fitting the orbit.

We fit the orbit using the following NS parameters from Camero Arranz et al. (2007):

MJD at periastron T = 52548.577

Orbital period $P = 12.66528 \pm 0.00051$

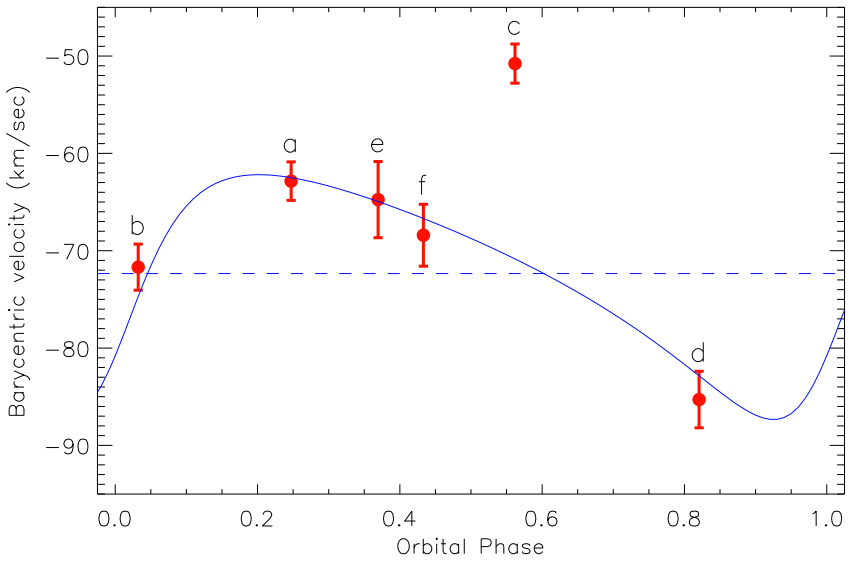

Figure 5.5. Radial velocity fit for SAX J2103.5+4545. I use a model atmosphere with T=29,000 K, $\log(g)$= 4.0, $v_{\rm rot}$ = 250 km s^{-1}. T_0 and phase 0 is defined as the periastron passage, corresponding to MJD 52548.577. Orbital period $P = 12.66528 \pm 0.00051$, $\omega_{\rm X} = 241° \pm 2°$, and $e = 0.40 \pm 0.02$ are held fixed at the best fit values by Camero Arranz et al. (2007). Note that $\omega_{\rm opt} = \omega_{\rm X} - 180°$. We calculate $\gamma = -72.3 \pm 1.3$ km s^{-1} and $k_{\rm opt} = -12.5 \pm 2.0$ km s^{-1}. The data point `c` corresponds is from 2009 July 31 and is excluded from the fit (see text).

Longitude of periastron ω $= 241° \pm 2°$

Eccentricity $e = 0.40 \pm 0.02$

For the B star, ω $= \omega$ $- 180°$. Using the five data points (`a, b, d, e, f`), we calculate γ $= -72.3 \pm 1.3$ km s^{-} and k $= -12.5 \pm 2.0$ km s^{-}, with χ $= 2.7$ for 3 degrees of freedom (Figure 5.5).

Camero Arranz et al. (2007) analyze the times of arrival of X-ray pulses and calculate a $\sin i = 80.81 \pm 0.67$ lt-s $= (2.42 \pm 0.02) \times 10$ km. Following Hilditch (2001, Equations 2.46, 2.50), we convert this to K :

$$K = \frac{2\pi}{(1-e)^{/}} \frac{a \sin i}{P} \tag{5.1}$$

If we measure P in days, $a \sin i$ in km and velocity in km s^{-} , we get:

$$K = \frac{7.27 \times 10^{-}}{(1-e)^{/}} \frac{a \sin i}{P} \quad (5.2)$$

$$= 152 \pm 6 \text{ km s}^{-} \quad (5.3)$$

For SAX J2103.5+4545, the uncertainty is dominated by the uncertainty in e. Using our best-fit value of K , we get $q = M /M = K /K = 0.082 \pm 0.013$. Assuming $M \approx 17.5$ M$_\odot$, we get $M = 1.44 \pm 0.14$. Assuming a reasonable range of B0 V star masses ($M = 17.5 \pm 2$ M$_\odot$), we conclude $M = 1.4 \pm 0.3$ M$_\odot$.

5.3 1H 2138+579

1H 2138+579 is a Be HMXB with a 66 s period transient X-ray pulsar. Observations by Bonnet-Bidaud & Mouchet (1998) revealed a B1.5 Ve primary with foreground extinction $A_V = 4.0 \pm 0.3$, corresponding to a distance $d = 3.8 \pm 0.6$ kpc. The measured projected rotational velocity $v \sin i = 460$ km s^{-} is close to the breakup velocities of B1-B2V stars

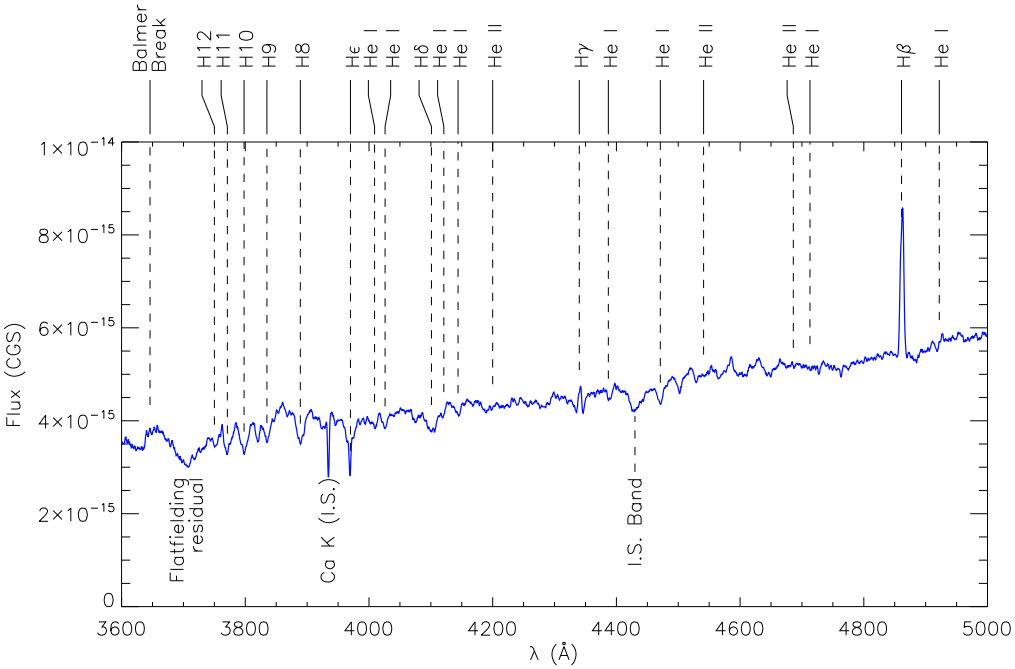

Figure 5.6. Blue side spectrum of the primary in 1H 2138+579. Major H and He lines are marked. Hβ is seen in emission, while Hγ has an emission core.

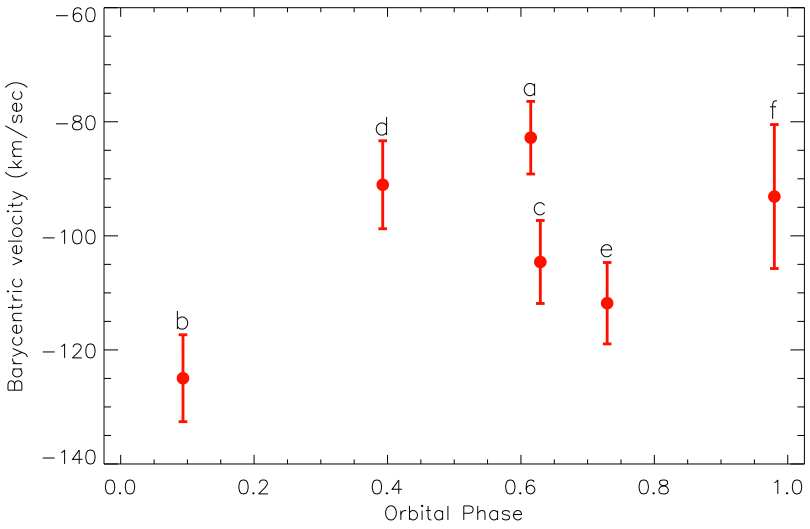

Figure 5.7. Radial velocity measurements for 1H 2138+579. I use a model atmosphere with T=24,000 K, log(g)= 4.0, $v_{\rm rot}$ = 500 km s^{-1}. The orbital period is P = 20.85 d. For this plot, data were folded with an arbitrarily selected heliocentric Julian date, T_0 = 2455015.866.

(Bonnet-Bidaud & Mouchet, 1998, and references therein). Assuming that the B star rotation is aligned with the orbit, they conclude $i > 65°$.

The blue side DBSP spectrum of 1H 2138+579 shows Hβ and Hγ in emission (Figure 5.6). The emission components likely arise from a "shell" or the disc around the Be star. Their strength varies from epoch to epoch, and the emission often fills up the broader absorption component from the stellar photosphere. He lines are relatively weak, as expected in a B1–B2 V star.

Typical B1–B2 V stars have T = 20000−26000 K, log(g) = 4.0 (Cox, 2000). For velocity measurements, we use Munari et al. (2005) model atmospheres with T = 24000 K, log(g) = 4.0, v = 500 km s^{-} and solar metallicity. We calculate the foreground extinction to be $A_V = 3.7 \pm 0.2$, and hold it fixed at $A_V = 3.7$ for RV measurements. The measured velocities do not show any clear orbital trend (Table 5.1, Figure 5.7).

Assuming M = 11 M$_\odot$, M = 1.5 M$_\odot$, $e = 0$ and $\sin i = 0.95$ ($i = 72°$), we expect K ≈ 20 km s^{-}, comparable to values we have measured for other objects. We attribute the non-detection of this signal to the variability of the H lines and the relatively low strength of other lines. Further analysis is under way to try and circumvent this limitation.

5.4 GRO J2058+42

GRO J2058+42 was discovered by the *Compton Gamma Ray Observatory* as a 198 s pulsar (Wilson et al., 1998). It is a Be HMXB with a 55.03 d period, at distance of 9.0 ± 1.3 kpc. The primary is a subgiant or a dwarf star of spectral class O9.5–B0 (Wilson et al., 2005), with projected rotation velocity $v \sin i = 240 \pm 50$ km s^{-} (Kzlolu et al., 2007). Assuming that the spin of the primary is aligned with the orbit, they constrain the inclination i to be $> 40°$ based on the break–up rotation velocity.

We obtained 36 spectra of GRO J2058+42 over the six epochs (Figure 5.8). We fit Munari et al. (2005) model atmospheres to our observed spectra and calculate $A_V = 4.4 \pm 0.4$, consistent with $A_V = 4.3 \pm 0.3$ measured by Kzlolu et al. (2007). The data are best fit by model atmospheres with $T = 33000 - 35000$ K and $\log(g) = 4.0$, as expected from the spectral type (Cox, 2000). Hence, we use model spectra with $T = 33000$ K, $\log(g) = 4.0$, $v = 250$ km s^{-} and solar metallicity for measuring radial velocities (Table 5.1).

On folding the data on the orbital period, it is evident that the orbit is not circular, as is the case with many Be HMXBs. The radial velocity solution to an eccentric orbit has two additional parameters: eccentricity e and argument of periastron ω. We choose not

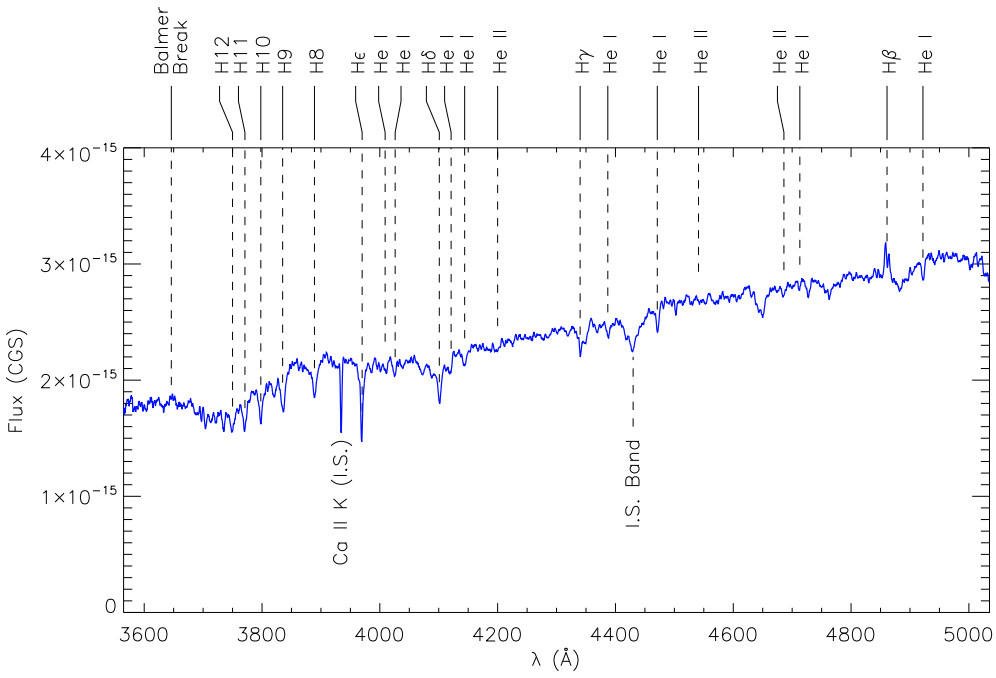

Figure 5.8. Blue side spectrum of the primary in GRO J2058+42. Major H and He lines are marked.

Chapter 6

Constraints on the Compact Object Mass in the Eclipsing HMXB XMMU J013236.7+303228

Varun B. Bhalerao,[a] Marten H. van Kerkwijk,[b] Fiona A. Harrison[a]

[a]Cahill Center for Astrophysics, California Institute of Technology, Pasadena, CA 91125, USA

[b]Department of Astronomy and Astrophysics, University of Toronto, 50St. George Street, Toronto, ON M5S 3H4, Canada.

Abstract

We present optical spectroscopic measurements of the eclipsing High Mass X-ray Binary XMMU J013236.7+303228 in M 33. Based on spectra taken at multiple epochs of the 1.73 d binary orbital period we determine physical as well as orbital parameters for the donor star. We find the donor to be a B1.5IV sub-giant with rough uncertainty of 0.5 spectral in spectral class and one luminosity class. The effective temperature is $T = 22,000-23,000$ K. From the luminosity, temperature and known distance to M33 we derive a radius of $R = 8.9 \pm 0.5\ R_{\odot}$. From the radial velocity measurements, we determine a velocity semi-amplitude of $K_{opt} = 63 \pm 12$ km s^{-} . Using the physical properties of the B-star determined from the optical spectrum, we estimate the star's mass to be $M = 11 \pm 1\ M_{\odot}$. Based on the X-ray spectrum, the compact companion is likely a neutron star, although no pulsations have yet

A version of this chapter has been submitted to the *Astrophysical Journal*. It is reproduced here with permission from AAS.

been detected. Using the spectroscopically derived B-star mass we find the neutron star companion mass to be $M = 2.0 \pm 0.4$ M$_\odot$, consistent with the neutron star mass in the HMXB Vela X-1, but heavier than the canonical value of 1.4 M$_\odot$ found for many millisecond pulsars. We attempt to use as an additional constraint that the B star radius inferred from temperature, flux, and distance, should equate the Roche radius, since the system accretes by Roche lobe overflow. This leads to substantially larger masses: $M < 2.7_{-\vdots}$ M$_\odot$ and $M < 18.9_{-\vdots}$ M$_\odot$. We find from known systems that by applying this technique in its simplest form the masses are consistently overestimated, and conclude that precise constraints require detailed modeling of the shape of the Roche surface.

6.1 Introduction

The range of possible neutron star masses depends on many factors, such as the initial mass of the progenitor's stellar core, the details of the explosion (in particular mass accretion as the explosion develops), subsequent mass accretion from a binary companion, and the pressure–density relation, or equation of state (EOS), of the neutron star matter. On the low-mass end, producing a neutron star requires the progenitor's core to exceed the Chandrasekhar mass, which depends on the uncertain electron fraction. Theoretical models place this minimum mass in the range $M \gtrsim 0.9$ – 1.3 M$_\odot$ (Timmes et al., 1996). The largest possible neutron star mass depends on the unknown physics determining the EOS—for example whether kaon condensates or strange matter can from in the interior (See, for example, Lattimer & Prakash, 2005). The highest-mass neutron star to date with an accurate measurement weighs in at 1.97 ± 0.04 $M_\odot$ (Demorest et al., 2010), which already rules out the presence of exotic hadronic matter a the nuclear saturation density (Demorest et al., 2010; Lattimer et al., 2010).

Testing the predictions of supernova models, binary evolution models, and finding objects at the extremes of the mass spectrum require determining neutron star masses in a variety of systems with differing progenitor masses and evolutionary history. Neutron stars accompanying either a high-mass star or another neutron star are thought to have accreted little to no matter over their lifetimes. In contrast, neutron stars in low-mass X-ray binaries and millisecond pulsars, typically in close orbits around a white dwarf, have undergone extended accretion periods that will make the current mass exceed that at birth. Different

types of binaries will also have different average neutron star progenitor masses.

High mass X-ray binaries (HMXBs)—binaries containing a neutron star and a massive ($\simeq$20 $M_\odot$) companion–are particularly interesting systems in which to pursue mass measurements. In most cases the neutron star progenitor will have been more massive than the observed donor star, yielding a relatively high-mass pre-supernova core. Furthermore, the NS mass will be close to the birth mass, since even for Eddington rates $\leq 0.1 M_\odot$ can be accreted in the ~ 10 yr lifetime of the OB companion. Indeed, among the five HMXB with reasonably secure masses, one (Vela X-1) has $M = 1.8$ $M_\odot$ (Barziv et al., 2001; Quaintrell et al., 2003), indicating that this neutron star may have been born heavy.

Determining NS masses in HMXBs is, however, difficult. In compact object (NS–NS, NS–white dwarf) binaries, highly precise mass measurements can be obtained from relativistic effects like the precession of periastron (Freire et al., 2008) or measurement of the Shapiro delay (Demorest et al., 2010). In HXMBs, however, accurate mass measurements are limited to eclipsing systems where orbital parameters for both the NS and its stellar companion can be measured. For the NS this is done through X-ray or radio pulse timing, and for the companion through radial velocity measurements derived from doppler shifts in the stellar lines. In the event pulsations are not detected, the NS mass can still be determined if good spectra are available to estimate the mass of the optical component. In rare cases where the distance to the binary is known, this provides an independent constraint on the physical scale of the system—for example by calculating the absolute magnitude of the components. However, calculating masses from such constraints is model dependent.

In this paper we present optical spectroscopic measurements of the donor star in the eclipsing HMXB XMMU J013236.7+303228 using the Low Resolution Imaging Spectrograph on the 10 m Keck-I telescope (LRIS; Oke et al., 1995) aimed at determining the mass of the compact companion. XMMU J013236.7+303228 was discovered by Pietsch et al. (2004) in their *XMM-Newton* survey of M 33. In follow-up observations, Pietsch et al. (2006) identified it as an eclipsing High Mass X-ray Binary with a 1.73 d period. The X-ray spectrum is hard, and the shape implies that the compact object is a neutron star. However we did not detect any pulsations in the X-ray data, so a black hole cannot be ruled out. Shporer et al. (2006) discovered an optical counterpart (Figure 6.1) which shows variability consistent with ellipsoidal modulation of the OB star. Given high quality spectra we are

able to obtain a spectroscopic mass for the donor, and therefore determine the compact object mass. Using the known distance to M33 combined with the B stars luminosity and temperature we derive a physical radius, which we equate with the Roche radius based on the observation that accretion is occurring via Roche lobe overflow. This provides an additional orbital constraint that we use to independently estimate the compact object mass.

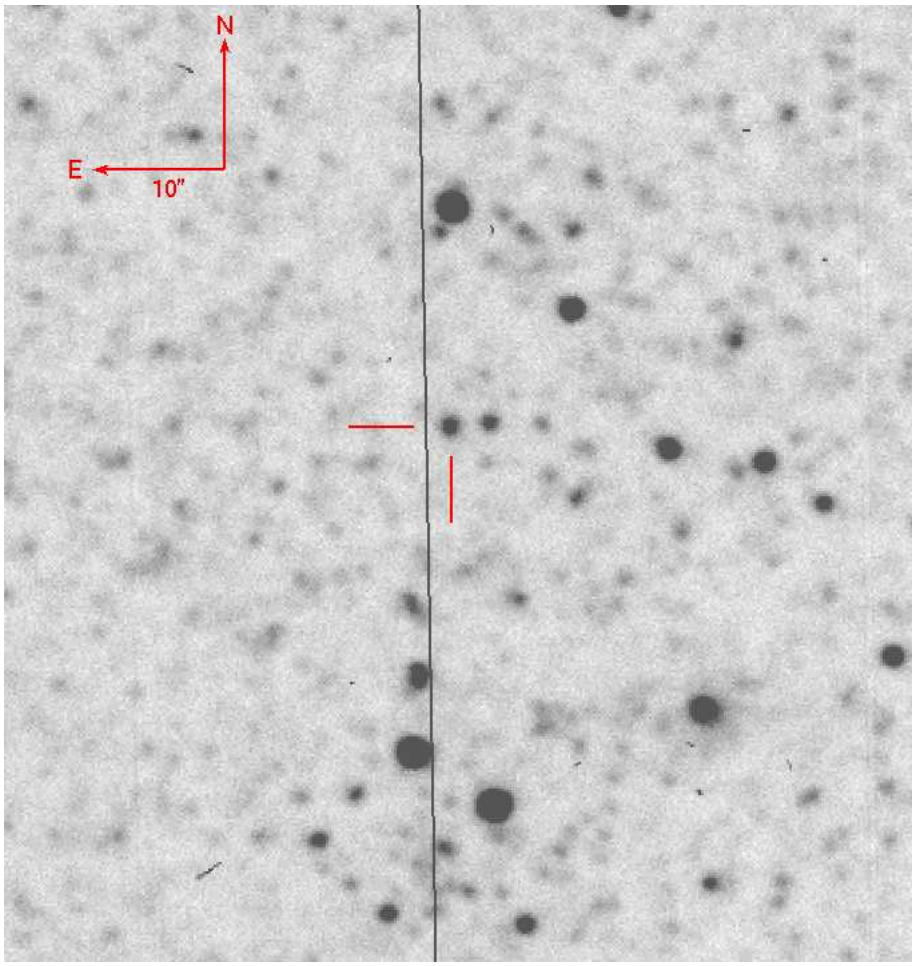

Figure 6.1. A V-band CFHT image showing the optical counterpart to XMMU J013236.7+303228, located at $\alpha = 01^{\rm h}32^{\rm m}36.^{\rm s}94$, $\delta = +30°32'28.''4$ (J2000). The image was obtained from CFHT online data archive, and a WCS was added using astrometry.net (Lang et al., 2010).

6.2 Observations And Data Reduction

We observed XMMU J013236.7+303228 on UT 2009 October 16 and October 17, with the Low Resolution Imaging Spectrograph on the 10 m Keck-I telescope (LRIS; Oke et al., 1995), with upgraded blue (McCarthy et al., 1998; Steidel et al., 2004) and red cameras (Rockosi et al., 2010), covering a wavelength range from 3,200 Å to 9,200 Å. We set up LRIS with the 600/4000 grism on the blue side and the 600/7500 grating on the red side, to get dispersions of 0.6 Å/pix and 0.8 Å/pix respectively Table 6.1. To maximize stability of the spectra, we used the "stationary rotator mode," where the instrument rotator was held fixed near zero degrees rather than tracking the parallactic angle while observing. Atmospheric dispersion was compensated for by the ADC (Atmospheric Dispersion Corrector). We acquired a total of 28 spectra of the target, with exposure times ranging from 300 to 1800 seconds. The spectrophotometric standard EG 247 was observed for flux calibration.

The data were reduced in `IRAF` [1]. The spectra were trimmed and bias subtracted using overscan regions. No flatfielding was applied. Cosmic rays were rejected using `L.A.Cosmic` (van Dokkum, 2001). Atmospheric lines are stable to tens of meters per second (Figueira et al., 2010), so the wavelength solution for the red side was derived using sky lines for each image. For the blue side, the wavelength solution was derived from arcs taken at the start of the night. The spectra were then rectified and transformed to make the sky lines perpendicular to the trace, to ensure proper sky subtraction. The wavelength solutions for arcs taken at various points during the night are consistent with each other to a tenth of a pixel, with only an offset between different arcs. We corrected for this offset after extracting the spectra, by using the 5577.34 Å [O `I`] line. The spectra were extracted with `APALL`, and fluxed with data for EG 247 and the standard `IRAF` lookup tables. We further tweaked the fluxing by using a EG 247 model spectrum from the HST Calibration Database Archive. We used just one standard spectrum per night, and enabled airmass correction in `IRAF` during flux calibration.

[1] http://iraf.noao.edu/ .

[2] ftp://ftp.stsci.edu/cdbs/current_calspec/ .

Table 6.1. Details of individual exposures

[a]	[b]	χ^2	[c]
	$^{-1}$		
-	±		
-	±		
-	±		
-	±		
-	±		
-	±		
-	±		
-	±		
-	±		
-	±		
-	±		
-	±		
-	±		
-	±		
-	±		
-	±		
-	±		
-	±		
-	±		
-	±		
-	±		
-	±		
-	±		
-	±		
-	±		
-	±		
-	±		
-	±		

″

°

[a]

[b] $^{-1}$

[c]

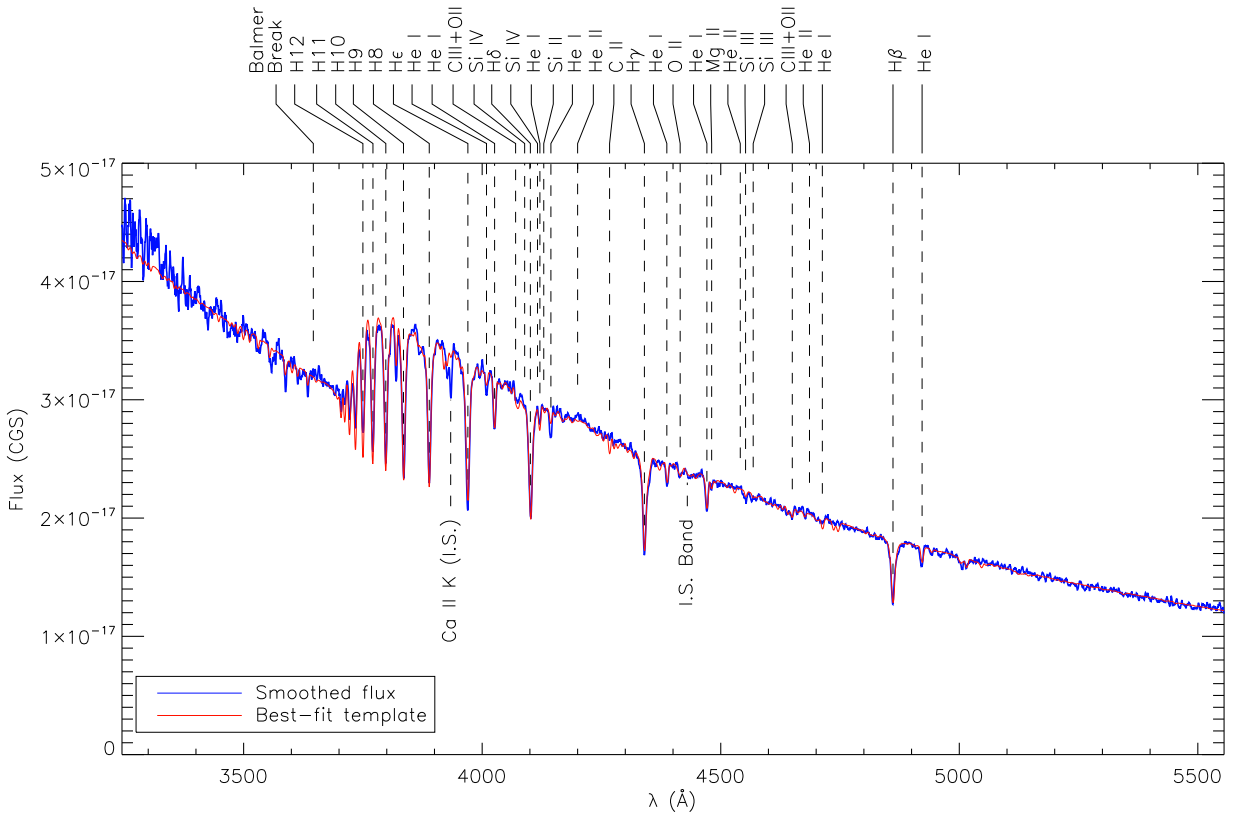

Figure 6.2. Observed spectrum and best-fit model for XMMU J013236.7+303228. The blue line is the average of the ten good spectra obtained on UT 2009 October 17, shifted to the rest wavelength using velocities from Table 6.1. The spectrum is smoothed with a 5 pixel (3 Å) boxcar for plotting. The red line is the best-fit template spectrum with $T = 22000$ K, $\log(g) = 3.5$, $v_{\rm rot} \sin i = 250$ km s^{-1}, solar metallicity. The template is reddened using $A_V = 0.395$, and scaled appropriately. Shifting the spectra to the rest frame blurs out the Ca II interstellar line and the 4430 Å interstellar band. The observed higher Balmer lines are less strong than those of the model, suggesting that the surface gravity is slightly higher than $\log g = 3.5$ (consistent with our estimated spectral type and with our fit results; see text).

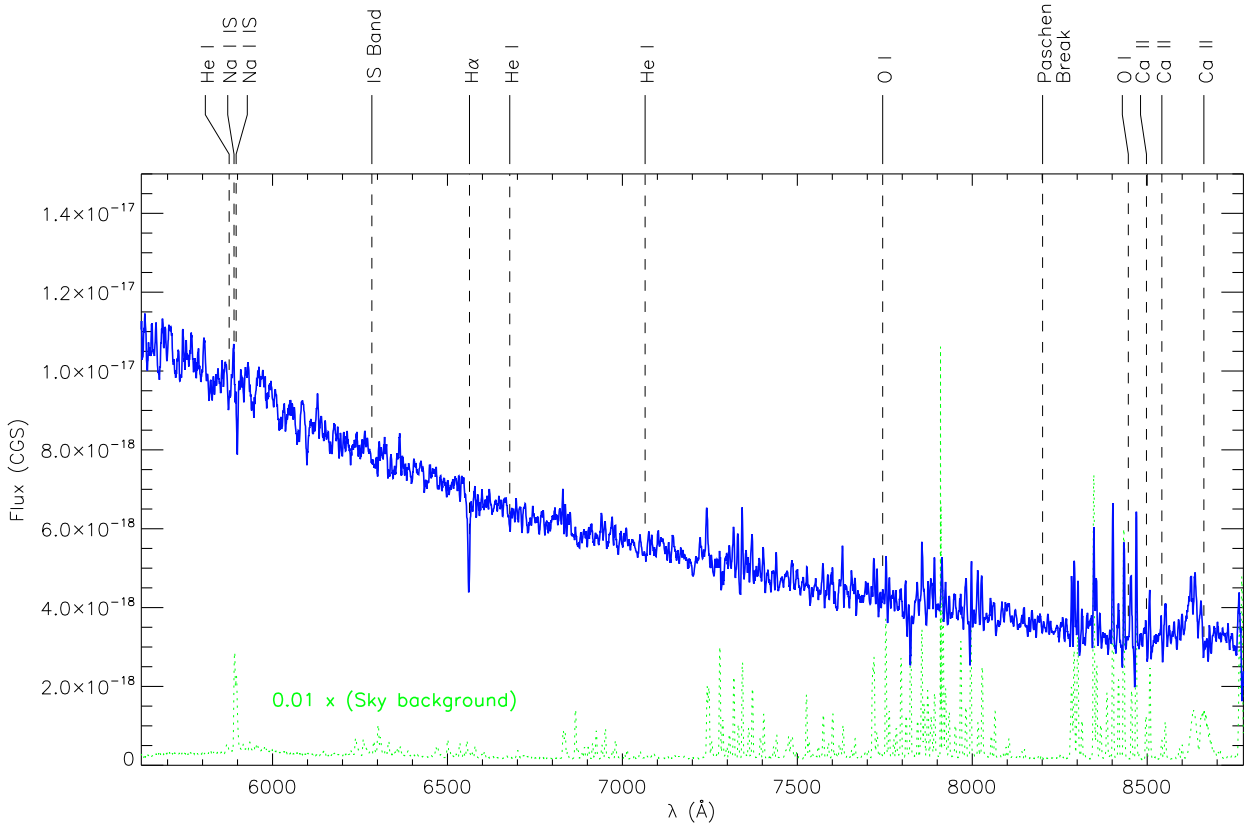

Figure 6.3. Observed red spectrum for XMMU J013236.7+303228. The blue line is the median combination of 48 spectra obtained on UT 2009 October 17, shifted to the rest wavelength using the velocity solution from Table 6.2. The flux axis differs from Figure 6.2. The spectrum is smoothed with a 5 pixel (4 Å) boxcar for plotting. The source is much fainter than the sky in this wavelength region. For reference, the green dashed line shows the extracted sky spectrum, scaled *down* by a factor of 100 for plotting. We do not use the red side spectra for any fitting.

The final spectrum is shown in Figures 6.2 & 6.3. The signal-to-noise ratio per pixel is >10 for most blue side spectra (Table 6.1). The first night, we experienced some tracking issues with the telescope, so the target did not remain well centered on the slit at all times. A similar problem was experienced for the first exposure on the next night, where the object was at a high airmass. In all following discussions, we reject some such spectra based on observing logs, and spectra with signal-to-noise ratio per pixel of <10 (Table 6.1).

6.3 Donor Star Parameters and Orbit

We determine the best-fit stellar parameters and orbital solution using an iterative technique. First, we estimate a spectral type for the primary (donor) from individual spectra. We use appropriate spectral templates to calculate the orbital solution (Section 6.3.2). Next, we shift spectra to the rest frame and combine them to get a higher quality spectrum. We calculate stellar parameters from this combined spectrum, and use a template spectrum with these refined parameters to recalculate the velocities. In this section, we describe the final iterations of both these steps.

6.3.1 Stellar Parameters

Based on photometry of XMMU J013236.7+303228, Pietsch et al. (2009) estimate that the companion is a 10.9 $M_\odot$ object with T = 33000 K and $\log(g) = 4.5$, with χ = 2.4 for their best-fit model. They then assume a distance of 795 kpc to M33, and calculate that the star has an absolute magnitude $M_V \sim -4.1$ and the line of sight extinction is $A_V = 0.6$, so derive a stellar radius of 8.0 $R_\odot$.

We deduce the spectral type by comparing our spectra to Walborn & Fitzpatrick (1990) and the Gray spectral atlas. The absence of He II lines (Figure 6.2) implies a spectral type later than O, while the relative strengths of the Mg II 4482 Å/He I 4471 Å lines point to a spectral type earlier than B3. The strength of He I lines, and a weak feature at 4420 Å indicate a spectral type around B1, for main sequence stars. A bump blueward of H8 3889 Å is characteristic of spectral type B2. The weakness of C III 4650 Å, and the relative strengths of C III/O II near 4650 Å refine the spectral type to between B1 and B2

[3] http://ned.ipac.caltech.edu/level5/Gray/frames.html .

for both dwarfs and giants. Finally, the weakness of Si IV Hδ 4101 Å, gives a spectral type of B1.5. To determine the luminosity class, we note that the O II 4415–4417 Å and Si III 4552 Å lines are present, but are weak as compared to He I 4387. We conclude that the donor is a B1.5IV star, with rough uncertainties of 0.5 spectral classes and one luminosity class.

Tabulated values of stellar parameters are usually provided for luminosity class III and V stars. For B1.5V stars, $T \approx 23000$ K, $\log(g) = 4.14$, and $M_V = -2.8$. For B1.5III stars, $T \approx 22000$ K, $\log(g) = 3.63$, and $M_V = -3.4$ (Cox, 2000). The B1.5IV target will have values intermediate to these. This inferred temperature is significantly cooler than $T \sim 33000$ K reported by Pietsch et al. (2009). However, the absence of He II lines at, e.g., 4541 and 4686 Å, clearly exclude such a high temperature.

The colors of a star depend on its temperature and surface gravity. These expected colors can be compared to the observed colors to calculate the reddening and extinction. The expected color is $(B-V) = -0.224$ for a 22000 K sub-giant star, and $(B-V) = -0.231$ for a 23000 K main sequence star (Bessell et al., 1998). From Pietsch et al. (2009), the mean magnitudes are $m_{g'} = 21.03 \pm 0.02$, $m_{r'} = 21.36 \pm 0.02$. Using the Jester et al. (2005) photometric transformations for blue, $U-B < 0$ stars, $m_V = 21.21 \pm 0.03$, $(B-V) = -0.09 \pm 0.04$. The color excess is $E(B-V) = (B-V) - (B-V) = 0.14 \pm 0.04$. Using the standard ratio of total-to-selective extinction, $R_V = 3.1$ we get $A_V = 0.43 \pm 0.12$. For comparison, the foreground extinction to M33 is $A_V = 0.22$.

We measure various stellar parameters by fitting our combined, fluxed spectrum with model atmospheres (taking into account the instrumental broadening; see Section 6.3.2). For a Roche lobe filling companion (discussed in Section 6.4), we expect a radius of 6–10 $R_\odot$, surface gravity $\log(g) \simeq 3.7$ (consistent with our luminosity class), and projected rotational velocity $v \sin i \simeq 250$ km s^{-} . We use these values as starting points to select model atmospheres from a grid calculated by Munari et al. (2005). These templates are calculated in steps of 0.5 dex in $\log(g)$, so we use models with $\log(g) = 3.5, 4.0$. For the initial fit, we assume $v \sin i = 250$ km s^{-} and solar metallicity. The only free parameters are a normalization and an extinction. We use extinction coefficients from Cox (2000), assuming $R_V = 3.1$. We find that the best-fit model for $\log(g) = 3.5$ has $T = 22100 \pm 40$ K and

[4] $V = g - 0.59(g-r) - 0.01 \pm 0.01$; $B - V = 0.90(g-r) + 0.21 \pm 0.03$.

$A_V = 0.401(3)$, with χ /DOF $= 1.13$ for 3600 degrees of freedom, while for $\log(g) = 4.0$, we get $T = 23500 \pm 50$ K and $A_V = 0.425(3)$ with χ /DOF $= 1.22$. The temperatures are consistent with those expected for a B1.5 subgiant star, and the extinction is within the range derived from photometric measurements. Pietsch et al. (2009) obtained a higher extinction for the target, which explains why they estimated the source temperature to be higher. Munari et al. (2005) templates are calculated in temperature steps of 1000 K in this range. For further analysis, we use the best-fit template: $\log(g) = 3.5$ and $T = 22000$ K. Since $\log(g)$ is slightly higher than this value, for completeness we also give results using the best fit template for $\log(g) = 4.0$, which has $T = 23000$ K. For both these templates, the best-fit extinction is $A_V = 0.395(3)$. We then keep T and $\log(g)$ constant and vary $v \sin i$. For both the $\log(g)$, T combinations, we measure $v \sin i = 260 \pm 5$ km s^{-} . Finally, using the same templates but with varying metallicity, we get the best fits for [M/H] $= 0$. The 0.5 dex steps in [M/H] are too large to formally fit for uncertainties.

Next, we calculate the luminosity of the object to obtain a radius–temperature relation. The distance modulus to M 33 is $(m - M)_{,\odot} = 24.54 \pm 0.06$ ($d = 809$ kpc; McConnachie et al., 2005; Freedman et al., 2001), which gives, accounting for the reddening of $A_V = 0.4$, $M_V = -3.74 \pm 0.07$. The bolometric luminosity of a star is related to its temperature and radius by $L \propto R^{} T^{}$. To obtain the visual luminosity, one must apply a temperature-dependent bolometric correction, $BC = M_{bol} - M_V$. Torres (2010) give formulae for bolometric correction as a power series in $\log(T)$. We calculate $BC = -2.11(-2.21)$ for $T = 22000(23000)$ K (which are consistent with Bessell et al. (1998) tables for main sequence stars.). After some basic algebra, we obtain:

$$5 \log\left(\frac{R}{R_\odot}\right) + 10 \log\left(\frac{T}{T_\odot}\right) + BC(T) = M_{,\odot} - m_V + (m - M)_{,\odot} + A_V \quad (6.1)$$
$$= 8.48 \pm 0.07.$$

Here, $M_{,\odot} = 4.75$ (Bessell et al., 1998). The resultant radius-temperature relationship is shown in Figure 6.4. For $T = 22000(23000)$ K, we infer $R = 9.1(8.7) \pm 0.3\ R_\odot$. The absolute magnitude and radius are both consistent with a B1.5 sub-giant.

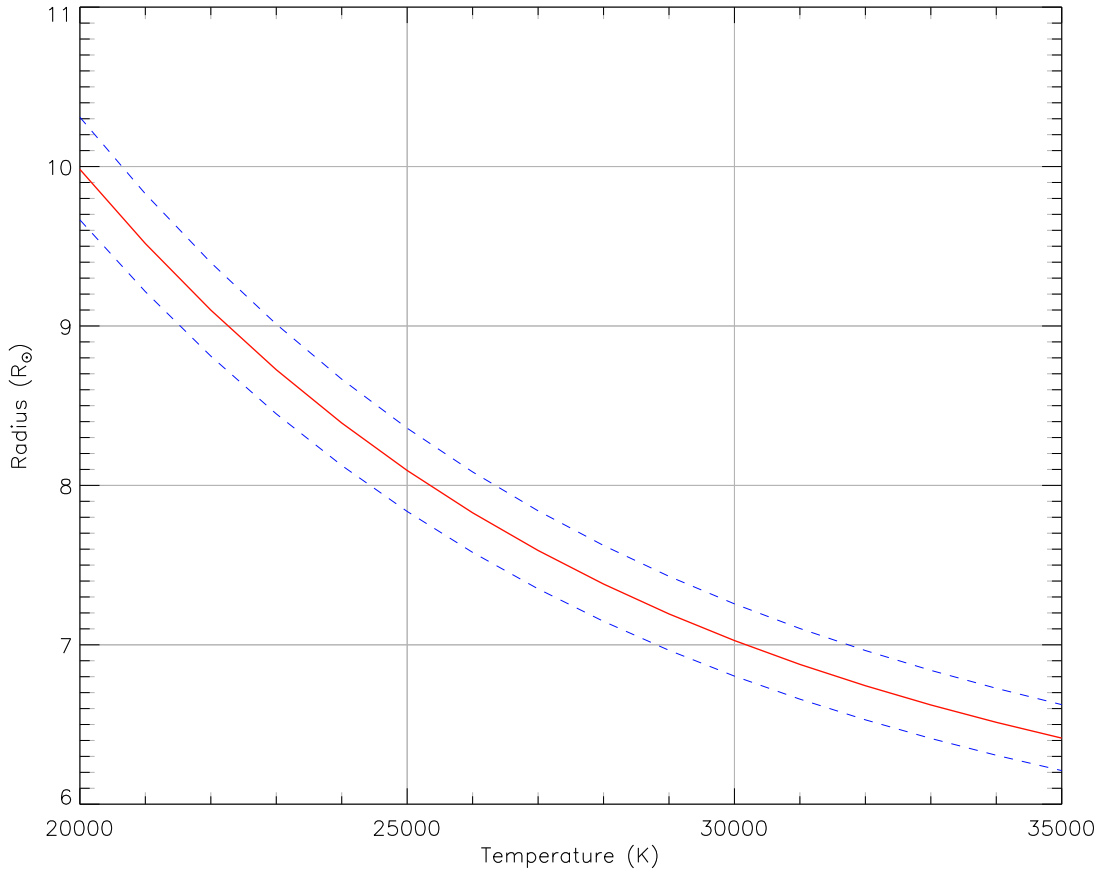

Figure 6.4. Radius–temperature constraint from the observed luminosity. We calculate the absolute visual magnitude from the apparent magnitude, distance modulus and best-fit extinction. We then apply a temperature-dependent bolometric correction to calculate the bolometric magnitude. For any given temperature in this range, the uncertainty in radius is about 3%.

6.3.2 Orbital Parameters

We measure the radial velocities of the B star using model stellar spectra by Munari et al. (2005), as follows. For each observed spectrum, we measure the seeing using the width of the spectral trace. We then generate an instrument response function by taking a Gaussian matched to the seeing, truncating it at the slit size, and convolving it with the pixel size. Fluxed synthetic spectra (templates) are convolved with this instrument response, then redshifted to a test velocity. Then we redden the template using the measured value of extinction, $A_V = 0.395$, with coefficients from Cox (2000). We use `IDL mpfit` (Markwardt, 2009) to calculate the reddening and normalization to match this spectrum with the observed spectrum, and measure the χ . By minimizing the χ over test velocities, we find the best-fit velocity and the error bars. This velocity is converted to a barycentric radial velocity using the `baryvel` routine in Astrolib (Landsman, 1993). Table 6.1 lists the radial velocities for all spectra, measured using the best-fit stellar template: $T = 22000$ K, $\log g = 3.5$, $[M/H] = 0.0$ and $v \quad \sin i = 250$ km s^{-} .

Red side spectra are not useful for radial velocity measurement for several reasons. The flux of the B star at redder wavelengths is lower than the blue wavelengths, and there are fewer spectral lines in this range. Also, the background noise is higher, from the large number of cosmic rays detected by the LRIS red side and from intrinsic sky emission. Hence, all further discussion omits red side spectra.

We calculate an orbital solution for the B star using these radial velocities. Owing to the short 1.73 d period of the system, we assume that the orbit must be circularized. The orbital solution is then given by:

$$v(t) = \gamma \quad + K \quad \sin\left(2\pi \frac{t - T}{P}\right) \tag{6.2}$$

where γ is the systemic velocity, K is the projected semi-amplitude of radial velocity, and T is the epoch of mid-eclipse. We adopt $T = 2453997.476 \pm 0.006$ from Pietsch et al. (2009). We obtain $\gamma \quad = -80 \pm 5$ km s^{-} , and $K \quad = 64 \pm 12$ km s^{-} . The best-fit has χ /DOF $= 5.1$ for 16 degrees of freedom, which is rather poor. We find that an additional error term $\Delta v = 15$ km s^{-} needs to be added in quadrature to our error estimates to

[5] http://www.ittvis.com/ProductServices/IDL.aspx

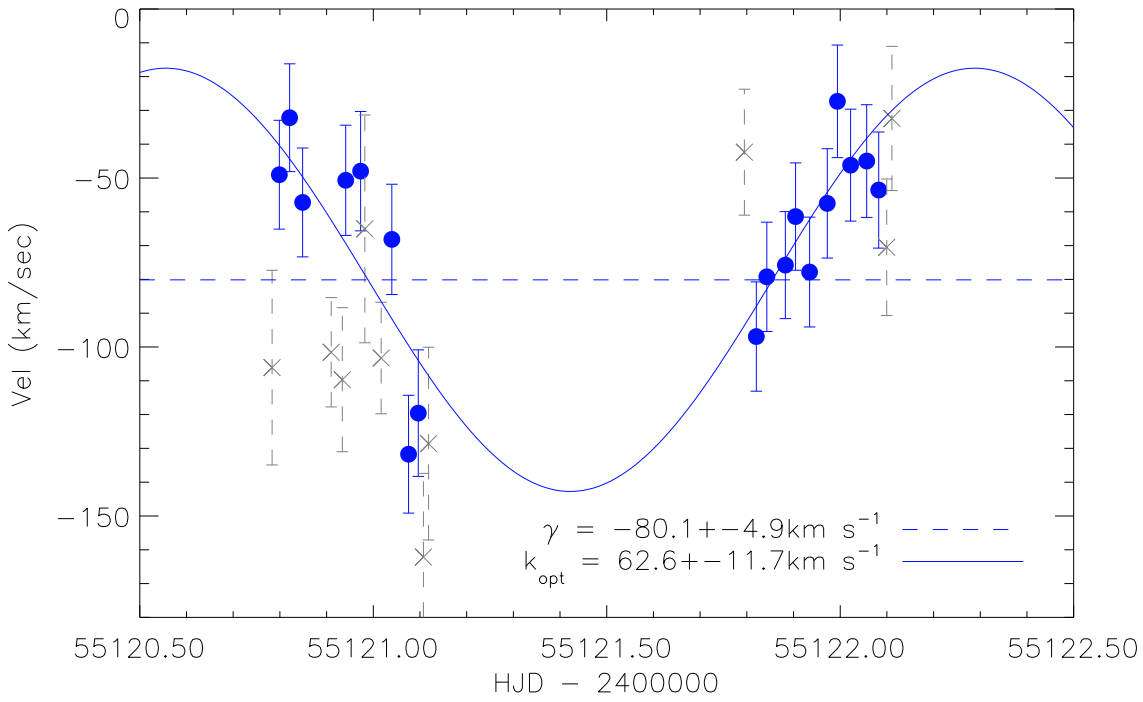

Figure 6.5. The radial velocity curve for XMMU J013236.7+303228. Solid blue circles denote points which were used in the final fit, and gray crosses are points which were rejected based on observing logs or a signal-to-noise ratio under 10 (Table 6.1). The solid blue curve is the best-fit orbital solution, and the dashed blue line is the mean systemic velocity.

obtain χ = 1. We attribute this to movement of the star on the slit. If the target has systematic offset of 0″.1 from the slit center over the entire 30 min exposure, it shifts the line centroids by about 0.45 pixels or 18 km s$^-$. For comparison, van Kerkwijk et al. (2011) find a similar scatter (13 km/s$^-$) in their observations of a reference star when using LRIS with a similar configuration (600/4000 grating, 0″.7 slit). Future observations should orient the spectrograph slit to obtain a reference star spectrum to correct for such an offset.

When we fit Equation 6.2 to data including the 15 km s$^-$ error in quadrature, we obtain γ = −80 ± 5 km s$^-$, and K = 63 ± 12 km s$^-$ (Figure 6.5, Table 6.2). For the epoch of observations, the uncertainty in phase is 0.019 d. If we allow T to vary, we get T , = 2453997.489 ± 0.019 (Heliocentric Julian Date), γ = −77.8 ± 2.1 km s$^-$, and K = 59 ± 5 km s$^-$. These values are consistent with those obtained using the Pietsch et al. (2009) ephemeris. Hence, for the rest of this paper, we simply assume their best-fit value for T .

Table 6.2. System parameters for XMMU J013236.7+303228

Property	Value
From Pietsch et al. (2004)	
Period (P)	1.732479 ±0.000027
HJD of mid-eclipse (T)	2453997.476 ±0.006
Eclipse half-angle (θ_e)	30°.6 ±1°.2
This work	
Systemic velocity (γ)	−80 ±5 km s^{-}
Velocity semi-amplitude (k)	63 ±12 km s^{-}
HJD of mid-eclipse (T)	2453997.489 ±0.019
Spectroscopically inferred	
OB star spectroscopic mass (M)	11 ±1 M$_\odot$
NS mass (M)	2.0 ±0.4 M$_\odot$
Distance-based calculations	
OB star mass (M)	18. $^{}_{}$ M$_\odot$
NS mass (M)	2.7 $^{}_{}$ M$_\odot$

To investigate the sensitivity of the result to the choice of the stellar template, we repeat the measurement with a variety of templates. We vary the temperature from O9 (33,000 K) to B3 (18,000 K) spectral classes. As before, we use templates with $\log(g) = 3.5, 4.0$; $v \sin i = 250$ km s^{-} and solar metallicity. Repeating the orbit calculations for each of these models, we find that the systemic velocity γ may change between models being fit: the extreme values are -77 ± 6 km s^{-} and -90 ± 5 km s^{-}, a 1.7-σ difference. We suspect that the reason for this variation is the difference in shape of the continuum, as the extinction was held constant in these fits. For hotter templates with a steeper continuum, the red side of a line has lower flux than the blue side, so lowest χ will be obtained at a slightly higher redshift, as seen. The magnitude of this effect should be independent of the intrinsic Doppler shift of the spectrum, and should not affect the velocity semi-amplitude K. This is indeed the case: K is constant irrespective of templates. The extreme values are 62 ± 12 km s^{-} and 63 ± 12 km s^{-}, differing by less than 0.1σ. Dynamical calculations depend only on K, hence they are robust to the selection of template.

6.4 Component Masses

The general method for accurately determining masses in X-ray binaries (Joss & Rappaport, 1984) requires measuring the orbit for both components, as well has having a constraint on the orbit inclination. In general, the mass (M) of a component is expressed in terms of five parameters: the orbital period P, the radial velocity semi-amplitude of the companion (K), the eccentricity e, the orbital inclination i and mass ratio $q = M/M$. The first three parameters can be readily obtained by characterizing the orbit of either component through pulse timing of the NS in the X-ray or radio, or by spectroscopically measuring the radial velocity of the optical companion at optical or infra-red wavelengths. Determining the mass ratio requires measuring orbital parameters for both components: $q = K/K$. In an eclipsing system, the inclination can be constrained to be nearly edge-on ($i \approx 90°$), with a lower limit derived from eclipse duration and Roche-lobe arguments. Using these measurements, masses of both components in the system can be directly determined without model assumptions (see for example, van der Meer et al., 2007; Mason et al., 2011b).

Because no pulsations have been detected from the compact object in XMMU J013236.7+303228, we need one more constraint in addition to the radial velocity semi-amplitude of the donor.

In Section 6.4.1 we use the spectroscopically inferred mass of the secondary to calculate mass of the secondary from the mass ratio. Because we know the distance to M33, and hence to XMMU J013236.7+303228, we can also estimate the physical size of the secondary from the distance, its luminosity and temperature. This provides a cross check on the mass determination derived from the spectroscopic donor mass (Section 6.4.2).

6.4.1 The Spectroscopic Method

In the following, we will denote the masses of the compact object and donor star by M and M respectively. The mass of the compact object (M) is related to the radial velocity of the B star (K) as follows:

$$M = \frac{K \quad P(1-e)^{/}}{2\pi G \sin i} \left(1+\frac{1}{q}\right) , \tag{6.3}$$

where $q = M /M$ is the ratio of masses, defined so that higher values of M relate to higher values of q. P is the orbital period of the binary, e is the eccentricity, and i is the inclination of the orbit. For eclipsing systems, the inclination is constrained by,

$$\sin i = \frac{\sqrt{1-\beta \ (R /a)}}{\cos\theta}, \tag{6.4}$$

where R is the volume radius of the Roche lobe, a is the semi-major axis, and β is the Roche lobe filling factor (Joss & Rappaport, 1984). For XMMU J013236.7+303228, the eclipse half-angle is $\theta = 30°.6 \pm 1°.2$ (Pietsch et al., 2009). Owing to the short orbital period, we assume that the orbit is circular and the B star rotation is completely synchronized with its orbit. For co-rotating stars, Eggleton (1983) expresses R /a in terms of q:

$$\frac{R}{a} = \frac{0.49q^{-/}}{0.6q^{-/} + \ln(1+q^{-/})}. \tag{6.5}$$

The constant, relatively high X-ray luminosity, sustained over the non-eclipsed parts of the orbit, strongly indicates that accretion is occurring via Roche lobe overflow. In Roche lobe overflow, matter flowing through the Lagrangian point may form a disc around the compact object before being accreted onto it. This disc can occult the compact object, causing periods of low X-ray luminosity. Both these characteristics are seen in the X-ray

lightcurves of XMMU J013236.7+303228 (Pietsch et al., 2009). If mass is being accreted onto an object in a spherically symmetric manner, the accretion rate is limited by the Eddington rate, $\dot{M}$ and the peak luminosity is L $/L_{\odot} = 3 \times 10$ $M/M_{\odot}$. For a 1.5 – 2.5 $M_{\odot}$ compact object, L $= 1.8-3\times10$ erg s^{-} . At its brightest, the source luminosity in the 0.2 – 4.5 keV band was 2.0×10 erg s^{-} —about $0.1L$. This luminosity was sustained throughout Chandra ObsID 6387, which covered about 0.72 d of the non-eclipsed orbit (Pietsch et al., 2009). Comparable flux was observed in the non-eclipsed parts of the orbit (0.73 d) in Chandra ObsID 6385. Such high luminosity sustained over significant parts of the orbit is not observed in wind-fed systems, which have typical luminosities an order of magnitude smaller. Further, the short 1.73 d orbital period is not consistent with Be X-ray binary or wind-fed systems. We conclude therefore the B star fills its Roche lobe.

The Roche lobe radius as a function of B star mass is plotted in Figure 6.6 for various neutron star masses. For a Roche-filling companion, we infer $3.6 \leq \log(g) \leq 3.8$. For a NS mass in the range 1.4–2.4 $M_{\odot}$ and B star mass 8–20 $M_{\odot}$, the B star radius lies in the range 6–10 $R_{\odot}$. Further, the assumed synchronous rotation requires the surface rotational velocity to be in the range 200 km s^{-} $\lesssim v$ $\lesssim$ 285 km s^{-} . These values are consistent with those derived in Section 6.3.1.

Figure 6.7 plots M as a function of M , calculated by solving Equations (6.3), (6.4) and (6.5) under known constraints. If we know M , we can calculate M . We use the physical properties of the primary (Section 6.3.1) to estimate the mass of the primary by comparing it with stellar evolutionary models, assuming that binary evolution has not drastically changed the mass-luminosity relation. First, we place the primary on a HR diagram (Figure 6.8) using models by Brott et al. (2011). We conservatively allow for a 0.5 mag error in luminosity. We also plot evolutionary tracks on a $\log(g)$-T figure, to utilize the stricter constraints on $\log(g)$ from Roche lobe arguments. From these plots, we see that the primary is approximately a 15 Myr old, ~ 11 $M_{\odot}$ star. This is consistent with the typical mass of a B1.5IV star (Cox, 2000).

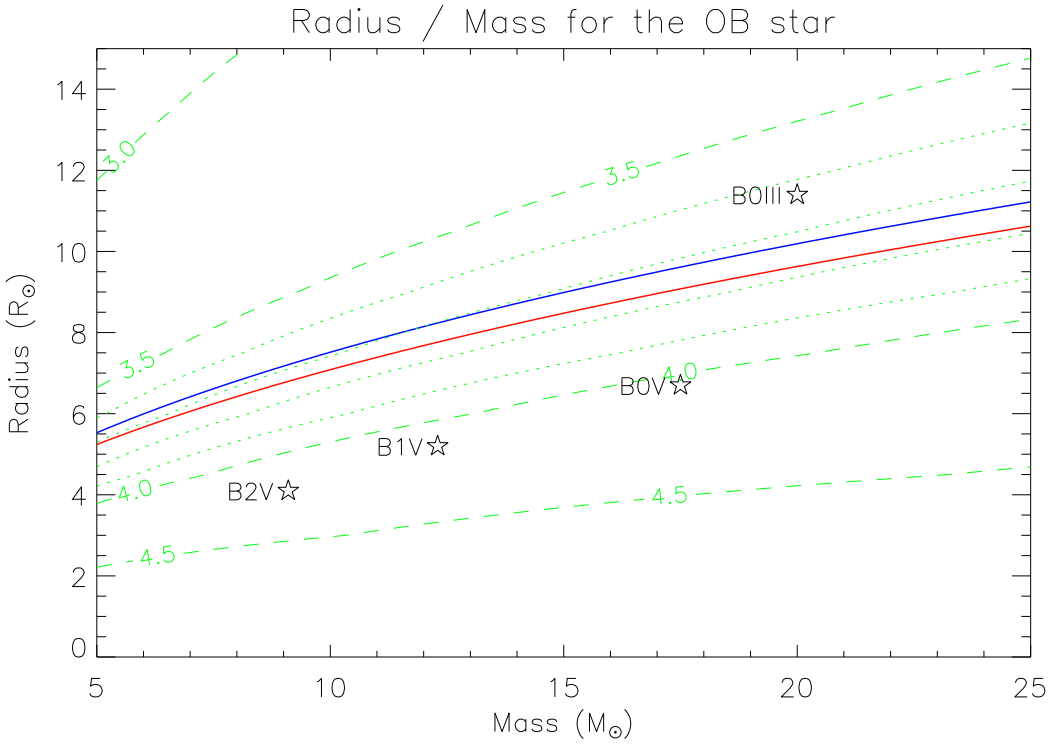

Figure 6.6. Mass–radius relation for the OB star. The solid lines show the Roche lobe radius for the OB star, assuming a 2.4 $M_\odot$ (upper blue line) and a 1.4 $M_\odot$ (lower red line) neutron star. The dashed green lines are contours for $\log(g)$ in steps of 0.5 dex, for which Munari et al. (2005) synthetic spectra are available. In the range $3.5 < \log(g) < 4.0$, dotted $\log(g)$ contours are separated by steps of 0.1 dex. The stars denote the masses and radii of typical isolated B stars.

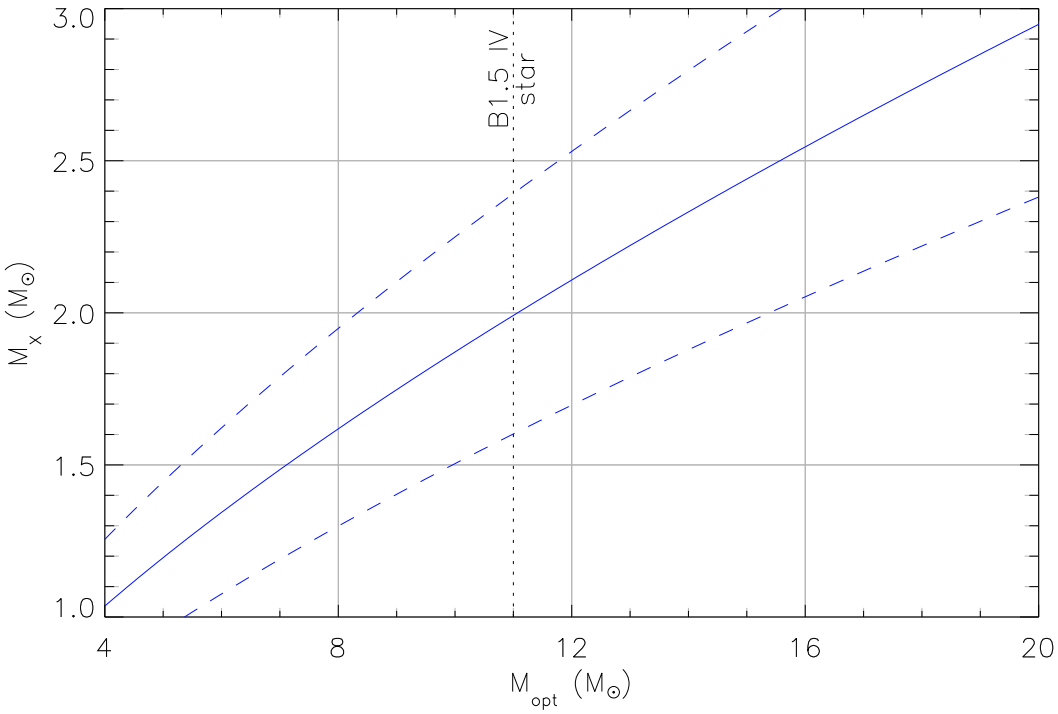

Figure 6.7. The solid blue line shows the compact object mass ($M_{\rm X}$) as a function of OB star mass ($M_{\rm opt}$). Dashed blue lines are $\pm$1-σ errors. The estimated mass of the B1.5IV primary is 11 $M_\odot$, marked by the vertical dotted line. The corresponding mass of the neutron star is 1.86 ± 0.16 $M_\odot$.

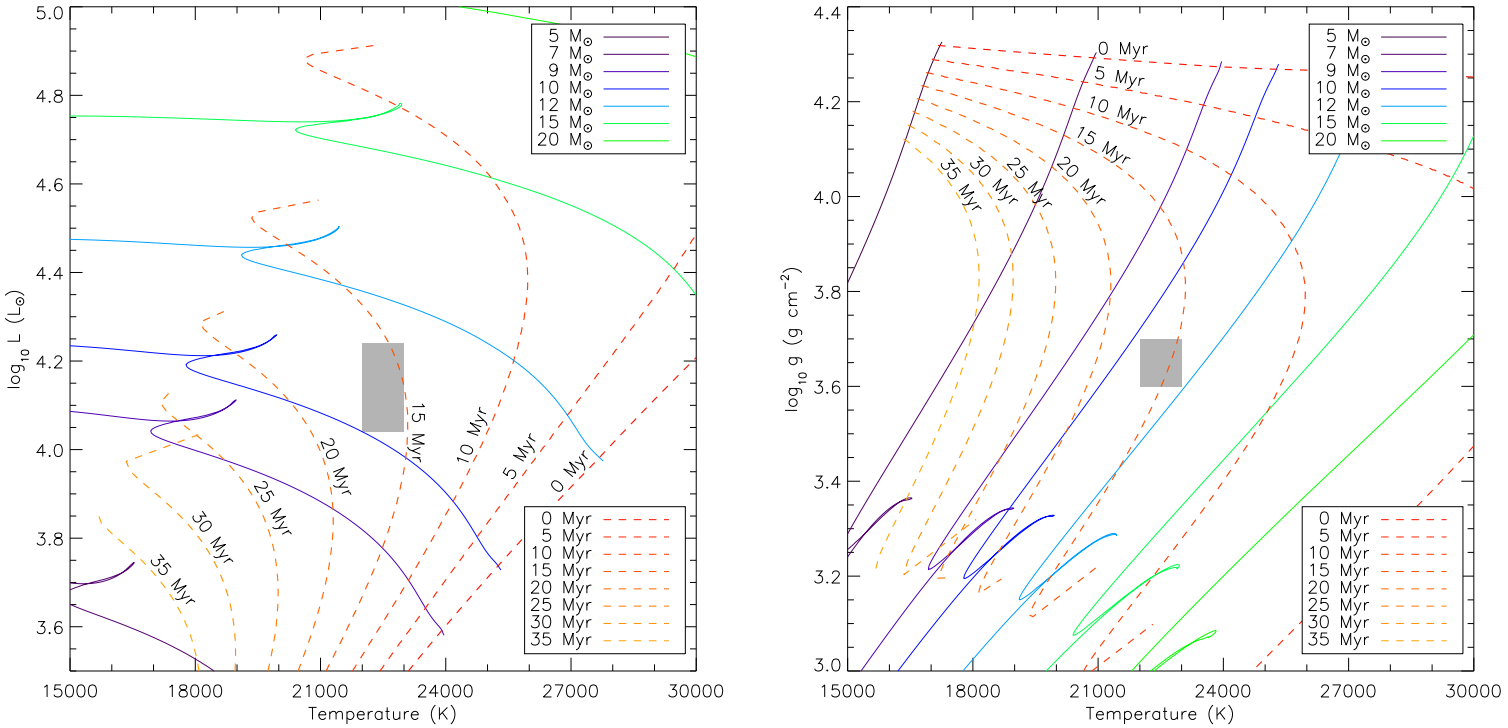

Figure 6.8. Evolutionary tracks and isochrones for massive stars (adapted from Brott et al., 2011). Left panel: the conventional HR diagram with luminosity and temperature. The primary star has 22000 K $\lesssim T \lesssim$ 23000 K. We calculate luminosity from the observed m_V, and allow a 0.5 mag offset to calculate the lower limit (see discussion in Section 6.4.1). This region is shown by a shaded gray box. Right panel: same, but plotted as $\log(g)$ versus T. $\log(g)$ for the primary is constrained from Roche lobe arguments (Section 6.3.1). From both panels, we see that the primary is consistent with a 11 $M_\odot$, 15 Myr object.

For M $= 11$ $M_\odot$, we calculate M $= 2.0 \pm 0.4$ $M_\odot$. From evolutionary tracks, we estimate that the uncertainty in M is $\sim$1 $M_\odot$ (Figure 6.8), corresponding to ΔM $= 0.12$, much smaller than the uncertainty arising from ΔK. Adding this in quadrature with with uncertainty in the M $- M$ conversion, we conclude M $= 2.0 \pm 0.4$ $M_\odot$.

6.4.2 Masses From Roche Lobe Constraints

In Section 6.3.1, we calculated the radius of the primary from its apparent magnitude, temperature and the distance to M33 (Equation (6.1)). Since the primary is filling its Roche lobe, the stellar radius is equal to the Roche lobe radius (R). This additional constraint can be used in Equations (6.3) – (6.5) to solve for M and M .

We calculate the probability density function (PDF) of component masses as follows. For every pair of assumed masses (M , M), we use the period P to calculate the semi-major axis a. Then we calculate R $/a$ from Equation (6.5) and substitute it into Equation (6.4) to calculate $\sin i$. Using P, a and $\sin i$ we calculate the expected semi-amplitude of the radial velocity:

$$K = \frac{2\pi a \sin i}{P} \frac{M}{(M + M)}. \tag{6.6}$$

Next, we calculate the probability for obtaining a certain value of R and K , given the measured radius R (Section 6.3.1) and K (Section 6.3.2):

$$P(R , K) = \exp\left(-\frac{(R - R)}{2 \cdot \Delta R}\right) \exp\left(-\frac{(K - K)}{2 \cdot \Delta K}\right) \tag{6.7}$$

Here, we are making a simplifying assumption that the Roche volume radius (Equation (6.5)) is same as the effective radius from photometry (Equation (6.1)). We convert this PDF to a probability density as a function of M , M by multiplying by the Jacobian $\partial(R, K)/\partial(M , M)$.

The results are shown in Figure 6.9. Red contours show the 68.3% and 95.4% confidence intervals for masses for the best-fit template ($\log(g) = 3.5$ and $T = 22000$ K). The panel on the left shows the PDF for M marginalized over M . Similarly, the lower panel shows the PDF for M , marginalized over M . In these panels, the the solid, dashed and dotted lines show the peak and 68.3%, 95.4% confidence intervals respectively. We obtain M $= 2.7_{-}^{\cdot}$ $M_\odot$, and M $= 18.1_{-}^{\cdot}$ $M_\odot$. For completeness, fits for the less likely scenario with $\log(g) = 4.0$ and $T = 23000$ K are shown in blue. In this case, M $= 2.5 \pm 0.6$ $M_\odot$,

M $= 16.1_{-}^{\cdot}$ $M_{\odot}$.

To test the validity of this technique, we apply it to two well-studied targets: LMC X-4 and SMC X-1. We find that the basic application of our method is overestimating the mass (Table 6.3). Part of this discrepancy is likely related to equating the Roche volume radius to the effective photometric radius (Equation (6.7)). The Roche volume radius (Equation (6.5)) is the radius of a sphere with the same volume as the Roche lobe of the star. The effective photometric radius (Equation (6.1)) is the radius of a sphere with the same surface area as the star. Since an ellipsoid has a larger surface area than a sphere of the same volume, the actual Roche volume radius will be smaller than the effective photometric radius. Using a larger radius for the Roche lobe increases the masses of both the components in the binary.

Putting it another way, if we use the Roche volume radius to calculate the brightness of the star, we will get a number lower than the observed brightness. A similar discrepancy is observed by Massey et al. (2012) in massive binaries in the LMC. They find that the absolute magnitude of LMC 172231 calculated using a spherical approximation is 0.45 mag fainter than observed, while for the triple system [ST92]2-28, the numbers are consistent within errors. Using system parameters derived by van der Meer et al. (2007), we find a similar offset of 0.45 mag for LMC X-4 and 0.2 mag for SMC X-1. If we incorporate this uncertainty by allowing offsets of 0–0.4 mag, we get M $= 2.2_{-}^{\cdot}$ $M_{\odot}$ and M $= 13\pm4$ $M_{\odot}$.

Thus while this method has potential, more detailed modeling of the primary is clearly required to accurately infer component masses.

6.5 Conclusion

From our spectroscopic measurements we find that the donor star in XMMU J013236.7+303228 is a B1.5IV sub-giant with effective temperature $T = 22000 - 23000$ K. The higher temperature, $T = 33000$ K reported by Pietsch et al. (2009) is inconsistent with the absence of He II lines at, e.g., 4541 and 4686 Å in our spectra. Assuming a circular orbit, we measure a mean systemic velocity γ $= -80 \pm 5$ km s^{-} and velocity semi-amplitude K $= 63 \pm 12$ km s^{-} for the B star. M33 is nearly face-on, with recession velocity of -179 km s^{-} (de Vaucouleurs et al., 1991) - so this binary seems to be moving away from the disc at 100 km s^{-} .

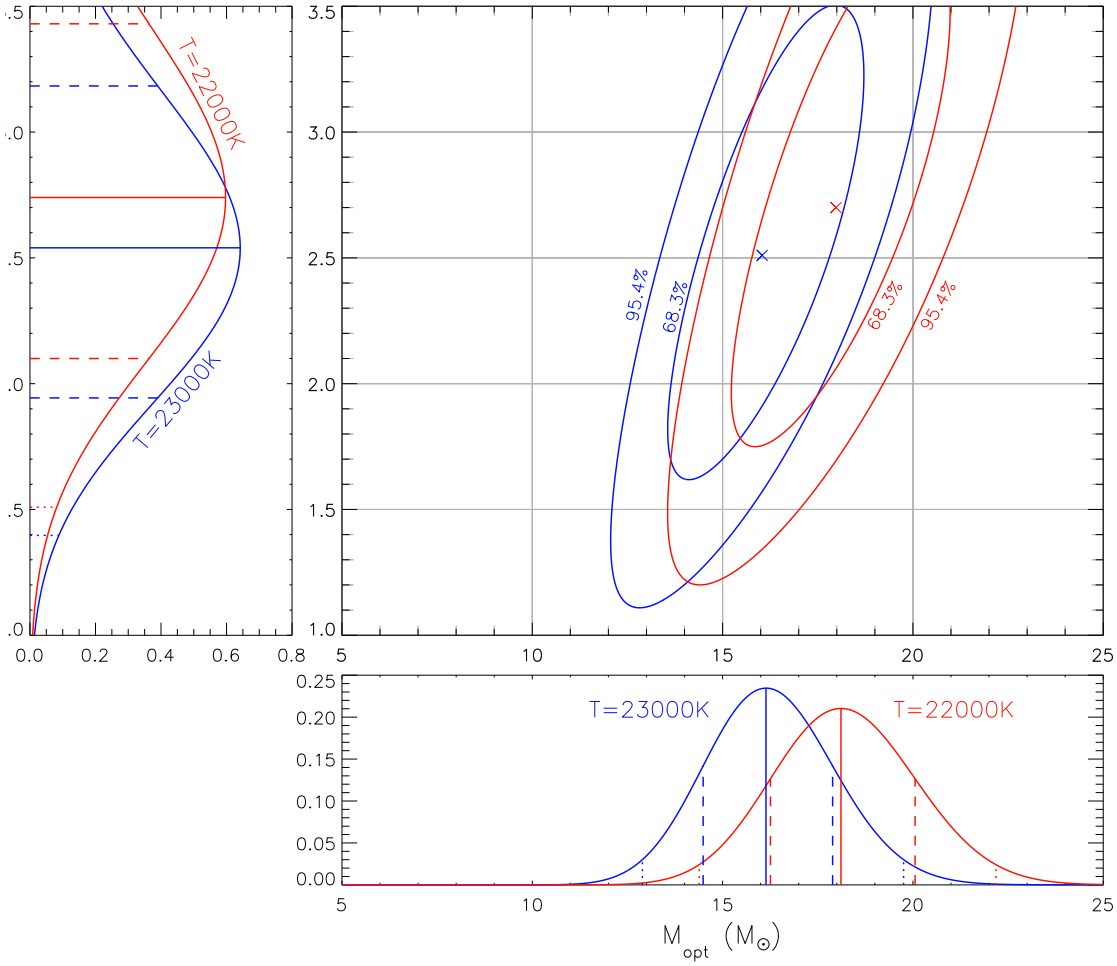

Figure 6.9. Probability density plot for neutron star mass ($M_{\rm X}$) as a function of OB star mass ($M_{\rm opt}$). Red contours show the 68.3%, 95.4% and 99.7% confidence intervals for masses using the best-fit template ($\log(g) = 3.5$ and $T = 22000$ K). The panel on the left shows the PDF for $M_{\rm X}$ marginalized over $M_{\rm opt}$. Similarly, the lower panel shows the PDF for $M_{\rm opt}$, marginalize over $M_{\rm X}$. In these panels, the the solid, dashed and dotted lines show the peak and 68.3%, 95.4% confidence intervals respectively. We obtain $M_{\rm X} = 2.61^{+0.32}_{-0.29}$ M$_\odot$, $M_{\rm opt} = 18.3^{+1.7}_{-1.6}$ M$_\odot$, and $M_{\rm X} > 2.0$ M$_\odot$ with 98.6% probability. Contours for the the less likely scenario with $\log(g) = 4.0$ and $T = 23000$ K are shown in blue. In this case, $M_{\rm X} = 2.43^{+0.30}_{-0.28}$ M$_\odot$, $M_{\rm opt} = 16.4^{+1.5}_{-1.4}$ M$_\odot$, and $M_{\rm X} > 2.0$ M$_\odot$ with 95.1% probability.

Table 6.3. System parameters for SMC X-1 and LMC X-4

Property	SMC X-1	LMC X-4
Period (P)	3.89 d	1.41 d
P	0.708 s	13.5 s
$a_X \sin i$ (lt-s)	53.4876 ±0.0004	26.343 ±0.016
Eclipse half-angle (θ_e)	26° – 30.5°	27° ±2°
Mean systemic velocity (γ)	−191 ±6 km s$^-$	306 ±10 km s$^-$
Velocity semi-amplitude (k)	20.2 ±1.1 km s$^-$	35.1 ±1.5 km s$^-$
Companion spectral type	B0I	O8III
Companion T	29000 K	35000 K
Distance (d)	60.6 ±1 kpc	49.4 ±1 kpc
Visual magnitude (m_V)	13.3 ±0.1	14.0 ±0.1
Extinction (A_V)	0.12 ±0.01	0.25 ±0.04
NS mass (M)		
van der Meer et al. (2007)	1.06 _ : M$_\odot$	1.25 _ : M$_\odot$
Our calculation	1.32 _ : M$_\odot$	2.05 _ : M$_\odot$
OB star mass (M)		
van der Meer et al. (2007)	≈ 15.7 M$_\odot$	≈ 14.5 M$_\odot$
Our calculation	21.1 _ : M$_\odot$	29.1 _ : M$_\odot$

Note. — Data from van der Meer et al. (2007).

Hilditch et al. (2005).

Freedman et al. (2001).

Conservative 0.1 mag errors assumed.

Foreground extinction to galaxy only. Error bars are approximate, the dominant uncertainty has been assigned to m_V.

Using the physical properties of the B star determined from our optical spectroscopy we find a mass for the donor of M $= 11$ M$_\odot$. This mass is based on stellar evolution models, and will be reasonably accurate so long as binary evolution has not significantly altered the mass-luminosity relation. However, it is difficult to test this assumption based on any available observations. Using this spectroscopic mass, we calculate the mass of the compact object, M $= 2.0 \pm 0.4$ M$_\odot$. This is higher than the canonical 1.4 M$_\odot$ for neutron stars, but comparable to masses of other neutron stars in X-ray binaries such as the HMXB Vela X$-$1 (1.88 ± 0.13 M$_\odot$; Barziv et al., 2001; Quaintrell et al., 2003) or the Low Mass X-ray binaries Cyg X$-$2 (1.71 ± 0.21 M$_\odot$; Casares et al., 2010) and 4U 1822$-$371 (1.96 ± 0.35 M$_\odot$; MunozDarias et al., 2005). Since no pulsations have been detected we have only indirect evidence, based on the X-ray spectrum, that the compact object is a neutron star. However, the mass we derive here is smaller than would be expected for a black hole.

Based on the stable X-ray flux, we infer that the donor is transferring mass to the neutron star by Roche lobe overflow. By equating the Roche lobe radius to physical radius of $R = 9.1(8.7) \pm 0.3$ $R_\odot$, derived from the known distance to M33, combined with the stellar luminosity and temperature, we derive an additional orbital constraint. From a first pass calculation with a spherical approximation for the shape of the primary we get M $= 2.7^{+}_{-}$ M$_\odot$ and M $= 18.1^{+}_{-}$ M$_\odot$. However, applying this technique to the well-studied binaries LMX X-4 and SMC X-1, both of which have measured component masses, we find this technique consistently overestimates the compact object mass. This is likely because the Roche surface is not spherical but elongated, which is not taken into account in our calculation. Future efforts to more accurately model the system geometry will improve the accuracy of this technique, which is applicable to Roche lobe overflow systems with known distances.

Acknowledgments

We thank Brian Grefenstette for helping with timing analyses of XMM data.

Some of the data presented herein were obtained at the W.M. Keck Observatory, which is operated as a scientific partnership among the California Institute of Technology, the University of California and the National Aeronautics and Space Administration. The Observatory was made possible by the generous financial support of the W.M. Keck Foun-

dation.

This research has made use of the NASA/IPAC Extragalactic Database (NED) which is operated by the Jet Propulsion Laboratory, California Institute of Technology, under contract with the National Aeronautics and Space Administration. This research has made use of NASA's Astrophysics Data System Bibliographic Services. This research used the facilities of the Canadian Astronomy Data Centre operated by the National Research Council of Canada with the support of the Canadian Space Agency.

Chapter 7

The White Dwarf Companion of a 2 $M_\odot$ Neutron Star

Varun B. Bhalerao and S. R. Kulkarni

Department of Astronomy, California Institute of Technology, Pasadena, CA 91125, USA

Abstract

We report the optical discovery of the companion to the 2 $M_\odot$ millisecond pulsar PSR J1614–2230. The optical colors show that the 0.5 $M_\odot$ companion is a 2.2 Gyr old He–CO white dwarf. We infer that $\dot{M}$ during the accretion phase is $< 10^{-}$ $\dot{M}$. We show that the pulsar was born with a spin close to its current value, well below the rebirth line. The spin-down parameters, the mass of the pulsar, and the age of the system challenge the simple recycling model for the formation of millisecond pulsars.

7.1 PSR J1614–2230

PSR J1614–2230, a 3.15 ms pulsar, was discovered in a radio survey of unidentified EGRET gamma ray sources using the Parkes Radio Telescope (Hessels et al., 2005). Subsequently, X-ray emission from *Newton XMM* (Roberts et al., 2007) and γ-ray emission from *Fermi*

A version of this chapter was published in the *Astrophysical Journal* (Bhalerao & Kulkarni, 2011). It is reproduced here with permission from AAS.

Gamma Ray Large Area Space Telescope (Abdo et al., 2010) was detected. Like most millisecond pulsars (MSPs), PSR J1614–2230 is in a binary system. The circular orbit is consistent with the pulsar having undergone mass transfer and spun up. The mass function derived from pulsar timing indicated a companion with mass $M > 0.4\ M_{\odot}$ (Hessels et al., 2005).

The system recently came into prominence when Demorest et al. (2010) reported the mass of the pulsar to be $1.97 \pm 0.04\ \mathrm{M}_{\odot}$. The detection of such a massive neutron star (NS) places very strong constraints on the equation of state of matter at extreme nuclear densities (see, for example, Lattimer & Prakash, 2004, 2005). The rather exquisite precision of this mass measurement was possible due to the orbit being almost perpendicular to the plane of the sky. As a result, the Shapiro delay caused by the companion is very large, resulting in a precise estimate of the mass of the companion, $M = 0.500 \pm 0.006\ M_{\odot}$. The 8.7 day orbital period is significantly shorter than ~ 120 days expected for a low-mass X-ray binary with such a massive secondary (Rappaport et al., 1995)—suggesting a peculiar evolutionary history for this binary.

Given the importance of the result of Demorest et al. (2010) additional verification or consistency checks of physical parameters of PSR J1614–2230 can be expected to be of some value. A $0.5\ \mathrm{M}_{\odot}$ white dwarf (WD) at the inferred distance of PSR J1614–2230 ($d \sim 1.2$ kpc), even if a few Gyr old, is within the reach of present-day optical telescopes. It is this search for the WD that constitutes the principal focus of this Letter.

7.2 Observations at the W. M. Keck Observatory

We observed PSR J1614–2230 (Figure 7.1) in g and R bands using the imaging mode of the Low Resolution Imaging Spectrograph (LRIS) on the 10 m Keck-I telescope (Oke et al., 1995), with upgraded red and blue cameras (McCarthy et al., 1998; Steidel et al., 2004). Several images were acquired at each target location, dithering the telescope by small amounts between each exposure. The observing conditions on UT 2010 May 15 were poor (seeing $1''.4$), so only data acquired on UT 2010 July 8 (R band seeing $0''.85$ FWHM) were used in this analysis. The total exposure on this night was 960 s in the R band and 1010 s in the g band. The plate scale is $0''.135$ pixel^{-} for both cameras

[1] http://www2.keck.hawaii.edu/inst/lris/lris-red-upgrade-notes.html

Table 7.1. Positions and magnitudes of reference stars

ID	RA $\alpha - 16\ 14$	Declination $\delta - (-22^\circ)$	m_R	m_g
A	36 .98(8)	29′18″.78(11)	17.94(8)	18.73(3)
B	36 .29(7)	29′31″.97(7)	17.71(8)	18.38(3)
C	35 .88(9)	30′18″.70(10)	19.76(10)	20.41(4)
D	34 .39(5)	30′12″.11(12)	19.15(8)	21.24(4)
E	35 .66	31′04″.17	21.38(9)	22.04(5)
F	34 .92(16)	30′59″.46(2)	20.18(9)	21.36(5)
G	37 .50	30′43″.69	20.71(8)	21.87(4)
Q	36 .47(7)	30′35″.90(4)	(Saturated)	17.20(3)
R	35 .92(2)	30′30″.45(1)	20.10(8)	20.94(4)
S	36 .50(10)	30′13″.93(13)	(Saturated)	17.75(3)

Note. — Stars A–G were used as reference stars for photometry. Right ascension and declination were obtained from USNO-B1.0 unless otherwise specified.

R band magnitudes calculated using SDSS magnitudes and Jester et al. (2005) transformation equations (Section 7.2). The numbers in parenthesis do not include a 0.03 mag uncertainty in absolute calibration due to the transformations.

Coordinates obtained from our final R-band science image. The World Coordinate System for this image was calculated using a total of 33 USNO-B1.0 stars (Section 7.2).

Table 7.2. Coordinates of PSR J1614–2230 at different epochs

Method	Epoch	Ecliptic Longitude (λ)	Ecliptic Latitude (β)	RA $\alpha - 16\ 14$	Declination $\delta - (-22°30')$
Timing	J2005.63	245.78827556(5)	−1.256744(2)	36 .5051(1)	31″.080(7)
Timing	J2000.00	245.78826025(12)	−1.256697(5)	36 .5034(2)	30″.904(19)
Timing	J2007.32	245.78828015(6)	−1.256758(2)	36 .5056(1)	31″.132(9)
Chandra	J2007.32	···	···	36 .50(15)	31″.33(20)
Timing	J2010.51	245.78828886(11)	−1.256785(5)	36 .5067(2)	31″.23(2)
LRIS	J2010.51	···	···	36 .50(16)	31″.72(20)

Note. — The proper motion of the pulsar as obtained from timing observations is $\mu_\lambda = 9.79(7)$ mas yr$^-$, $\mu_\beta = -30(3)$ mas yr$^-$. This proper motion is used to estimate the ecliptic coordinates of the pulsar at the epoch of the *Chandra* and LRIS observations. The right ascension and declination are calculated from ecliptic coordinates using the `Euler` program in `IDL`. The equinox in all cases is J2000.

Bore-sight corrected coordinates. The target and the reference source "E" are detected in the *Chandra* image. We extract source coordinates using `celldetect`. We assume that the *Chandra* coordinate system and our R-band coordinate solution are related by a simple offset with no rotation. Using the X-ray and R-band coordinates of source E, we calculate that the offset is $\alpha_X - \alpha_R = 0''.21$, $\delta_X - \delta_R = -0''.20$ and correct the target position using this offset.

The images were processed using `IRAF`. After bias correction and flat fielding, cosmic rays were rejected using `L.A.Cosmic` (van Dokkum, 2001). The images were then aligned with `xregister` and averaged to produce the final image for each band (see Figure 7.1). A World Coordinate System was calculated using USNO-B1.0 stars in the field, with the `imcoords` package. Using 33 stars in the field, for the final R-band image we obtained an RMS error of $0''.14$ in right ascension (R.A.) and $0''.20$ in declination, adding up to a radial error of $0''.24$. For the final g-band image, the residuals were $0''.13$ and $0''.18$ for R.A. and declination, respectively, giving a total error of $0''.22$.

We measured fluxes with aperture photometry using the `IDL APPHOT` package. For each night, we measured the seeing (FWHM) and set the aperture to one seeing radius (Mighell, 1999). We extracted the sky from an annulus 5–10 seeing radii wide. We had observed nearby a Sloan Digital Sky Survey (SDSS; York et al., 2000) field[2] with the same settings as the science field. The calibration field was observed immediately after the science exposures, and had airmass 1.4 as compared to 1.6 for the target. We used the magnitudes of six stars from that field to calculate the photometric zero point and calibrated six reference stars in the science field (Figure 7.1, Table 7.1). R band magnitudes were calculated using photometric transformations[3] prescribed by Jester et al. (2005) for stars with $R_c - I_c < 1.15$. The typical uncertainty in g-band magnitudes for stars with $m_g \sim 20$ is 0.03 mag. In R band we have $\Delta m_R = 0.07$ for $m_R \sim 20$, including the uncertainty in the transformations.

7.3 Detection of an Optical Counterpart

In the vicinity of the nominal pulsar position, we find a faint source (labeled "P") in the R band (Figure 7.1). We do not detect anything within $1''$ of the target in the g band. The optical coordinates of this source, the timing position of the pulsar and a proposed X-ray counterpart are summarized in Table 7.2. To compare this with the source location, we first have to correct for the 33 mas yr$^-$ proper motion of the source. The LRIS source P is about $0''.50$ South of the pulsar position (extrapolated for the epoch of LRIS observations). Given the $0''.24$ (1-σ) astrometric uncertainty of the optical images, this position is consistent with the location of the pulsar.

[2]Calibration SDSS field: $\alpha = 17^{\rm h}19^{\rm m}10^{\rm s}.10$, $\delta = -14^\circ 38' 46''.0$.

[3]Photometric transforms: $V = g - 0.59(g - r) - 0.01 \pm 0.01$ and $V - R = 1.09(r - i) + 0.22 \pm 0.03$.

The density of objects brighter than star P in this field is 0.02 arcsecond^{-} . Using the 0″.85 seeing FWHM as the mean diameter of stars, we calculate a false identification probability of 1%. The excellent astrometric coincidence and the low probability of chance coincidence embolden us to suggest that star P is the optical counterpart of PSR J1614–2230.

Counterpart P is located only 4″.2 from the 16.3 mag star USNO-B1.0 0674-0429635, and is contaminated by the flux in the wings of its point-spread function. The proximity to this bright source will bias both the photometry and the astrometry of the counterpart. To calculate the bias, we injected fake Gaussian sources with FWHM matched to the seeing and brightness comparable to the faint object. We then measured the coordinates and magnitude of the injected source using the same procedure as for the faint object. We find that for separations $\approx 4''.2$, the recovered position is systematically pulled towards the bright star by 0″.1–0″.2. This is small enough that we do not apply this correction. The same exercise led us to derive the photometric bias. The de-biased R-band magnitude of P is $m_R = 24.3 \pm 0.1$.

To infer properties of the WD, we need to calculate its absolute magnitude. To calculate the optical extinction, we assume that the ratio N /N_e is constant along the line of sight in the direction of PSR J1614–2230. The dispersion measure (DM) for PSR J1614–2230 is 34.5 pc cm^{-} (Demorest et al., 2010), and the total DM in this direction is 104 pc cm^{-} (Cordes & Lazio, 2002)—about a factor of three higher than the pulsar DM. This implies that the pulsar is behind approximately one third of the galactic absorbing column. We can then scale the total R band extinction in this direction ($A_{R,}$ = 0.65; Schlegel et al., 1998) to get $A_R = 0.22$. We assume λ = 0.47 μm for the g band , and use the standard reddening law with $R_V = 3.1$ to get $A_g = 0.34$ (Cox, 2000).

Demorest et al. (2010) use the DM to estimate that PSR J1614–2230 is at a distance d = 1.2 kpc. For this distance, the extinction-corrected R-band absolute magnitude is $M_R = 13.7 \pm 0.1$. Furthermore, they place a lower limit of 900 pc on the distance, using pulsar parallax from timing measurements. The corresponding absolute magnitude is $M_R = 14.3 \pm 0.1$.

[4]http://www.sdss.org/dr6/instruments/imager/index.html#filters

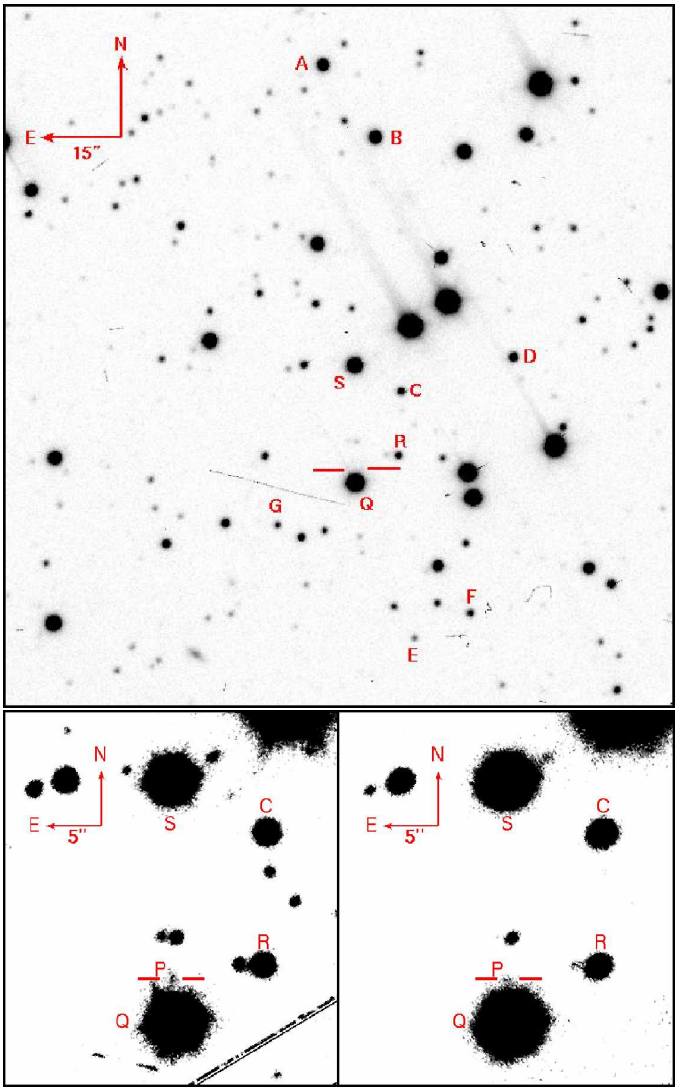

Figure 7.1. Top: R band LRIS image of the PSR J1614–2230 field. The expected location of the target for epoch 2010.52 is shown by two horizontal lines just below the center of the image. The CCD shows considerable blooming in rows and columns around bright stars. The hexagonal mirror shape gives six diffraction spikes separated by 60°. To avoid contamination of the target by these artifacts from the bright star Q, we set the position angle to 300°. Bottom: R-band (left) and g-band (right) images of PSR J1614–2230. The target (P) is detected in the R band at $\alpha = 16^{\rm h}14^{\rm m}36^{\rm s}.50$, $\delta = -22°30'31''.72$ and is marked with thick horizontal lines. There is a $0''.33$ offset between the expected and observed positions of the target (Table 7.2). The target is not detected in the g-band, but the R band location is marked for reference. The diagonal streak in the R image is a bad CCD column.

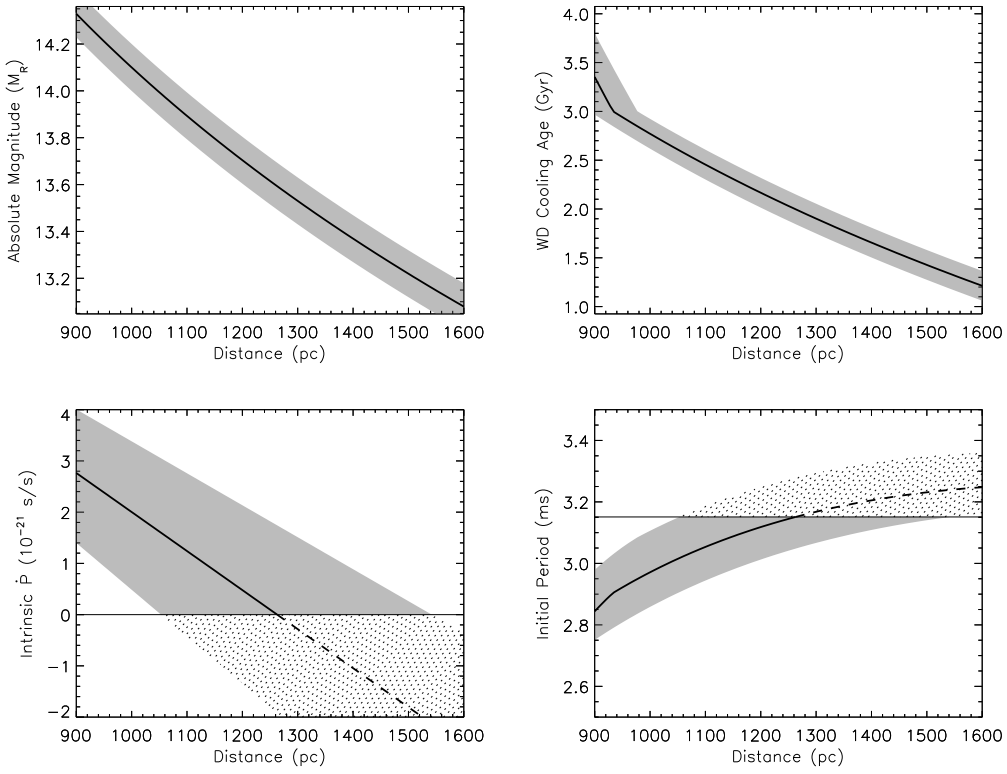

Figure 7.2. Inferred parameters for PSR J1614–2230 as a function of distance. The gray or dotted regions show the error bars on each parameter. Top left: The absolute R-band magnitude of the WD. Top right: WD cooling age inferred from Chabrier et al. (2000). The kink at 3 Gyr may be a result of granularity of the tables. Bottom left: the intrinsic period derivative ($\dot{P}$) in the pulsar frame, corrected for the Shklovskii effect. Since the pulsar cannot be spinning up, the values of $\dot{P} < 0$ are unphysical and are shown as the dotted area. The maximum distance to the pulsar is inferred to be 1540 pc. Lower right: the initial spin period of the pulsar. Birth periods slower than the current period are excluded.

7.4 Pulsar age and birth spin period

The measured mass (0.5 $M_\odot$) and the inferred absolute magnitude ($M_R \approx 13.7$) when applied to WD cooling models (Chabrier et al., 2000) lead to an age of $\tau \sim 2.2$ Gyr. For such a WD, the expected absolute magnitude in other bands is $M_B = 14.6$ and $M_V = 14.1$. This gives $m_g \approx 25.0$, consistent with our non detection.

As per the standard evolutionary model for MSPs, the NS in PSR J1614–2230 was spun up by accretion from a low- or intermediate-mass companion star. The accretion stopped when the companion decoupled from its Roche lobe and became a WD. At this point, the MSP started spinning down by radiating energy. The spin-down age of the MSP is thus equal to the cooling down age of the WD.

The period of the pulsar at birth (P), its spin-down age (τ), present-day period (P) and period derivative ($\dot{P}$) are related to each other as follows:

$$\tau = \frac{P}{(n-1)\dot{P}} \left[1 - \left(\frac{P}{P} \right)^{n-} \right] \tag{7.1}$$

where n is the "braking index" for the pulsar, with $n = 3$ appropriate for a dipole radiating into vacuum. Thus, the period at birth is given by

$$P = P \left[1 - \frac{\tau \dot{P}(n-1)}{P} \right]^{/\, n-} \tag{7.2}$$

The measured period derivative of a pulsar ($\dot{P}$) is always higher than its true period derivative ($\dot{P}$) owing to transverse motion (Shklovskii, 1970). The corrected period derivative is $\dot{P} = \dot{P} - P\mu\, d/c$, where d is the distance and μ is the proper motion. Demorest et al. (2010) measure $\mu = 32(3)$ mas yr$^-$ for PSR J1614–2230. Using the nominal distance $d = 1.2$ kpc, $\dot{P} = 4.8 \times 10^-$ s s$^-$.

The DM inferred distance is quite uncertain, so it is useful to consider the dependence of all parameters on distance. Figure 7.2 shows the range of values for the R-band absolute magnitude (M_R), the WD cooling age (τ), the intrinsic period derivative in the pulsar's frame ($\dot{P}$) and the initial spin period (P). Since there is no energy injection to the pulsar now, it must be currently spinning down. This implies $\dot{P} \geq 0$ and allows us to calculate an upper limit on the distance to the pulsar: d = 1540 pc (1-σ). The last panel in

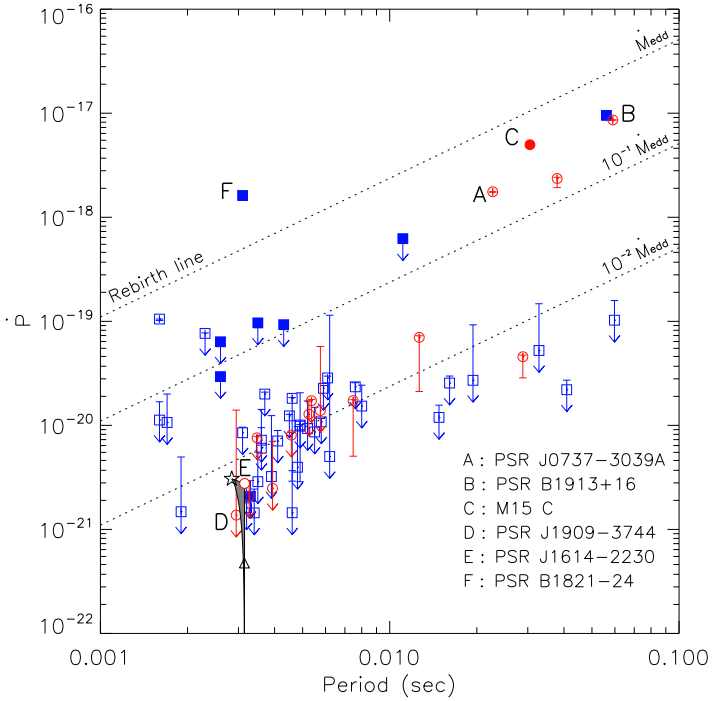

Figure 7.3. Pulsar P–$\dot{P}$ diagram. Period derivatives are corrected for the Shklovskii effect. Some interesting systems are labeled. Filled symbols are pulsars in globular clusters, whose $\dot{P}$ may be affected by the dense environment. Circles denote NS binaries with mass measurements. The dashed lines are the pulsar rebirth lines $\dot{P} = (\dot{M}/\dot{M}_{\rm edd})1.1 \times 10^{-15}\ {\rm s}^{-4/3} P^{4/3}$ (Arzoumanian et al., 1999) for $\dot{M}/\dot{M}_{\rm edd} = 1$, 10^{-1} and 10^{-2}. The location of PSR J1614–2230 on this plot depends on the distance (see Section 7.4). Were the pulsar to be at 900 pc, it would be born at the star symbol and evolve toward its present-day location, the hollow circle marked "E". If instead it is at 1200 pc, the birth location is shown by the upward triangle, which also coincides with its present-day location. The solid curve passing through the star and the upward triangle denotes all possible birth locations for PSR J1614–2230. The system evolves through the shaded gray area to its present-day location on the vertical line through E and the upward triangle.

Figure 7.2 shows $P \geq 2.75$ ms. We conclude that the pulsar in PSR J1614–2230 must have been born with a period close to the current observed value.

The birth spin period of a NS is governed by an equilibrium between the ram pressure of the accreting material and the magnetic field. NSs spun up by accretion at the Eddington rate ($\dot{M}$) are reborn as MSPs on the "rebirth line" (Arzoumanian et al., 1999). Figure 7.3 shows this rebirth line on a P–$\dot{P}$ diagram, along with current positions of various pulsars from the ATNF database (Manchester et al., 2005). Also shown are rebirth lines for pulsars accreting at 10^{-} $\dot{M}$ and 10^{-} $\dot{M}$. For a pulsar radiating as a dipole, the $P\dot{P}$ product remains constant through its lifetime. Thus, we can calculate the initial spin-down rate of the pulsar: $\dot{P} = P\dot{P}/P$, where P comes from Equation 7.2. If PSR J1614–2230 is at 900 pc, then it would have been born with $\dot{P} = 3.1 \times 10^{-}$ s s^{-} and $P = 2.84$ ms. This value is indicated with a star. The pulsar then evolves toward the lower right, to the circle marked "E". Similarly, the birth parameters for the pulsar assuming $d = 1.2$ kpc are shown by the upward triangle—it is nearly coincident with the current parameters of the pulsar for this distance. Other possible birth locations for the pulsar lie along the solid line passing through the star and triangle. The gray region shows all possible positions that PSR J1614–2230 can have occupied in its lifetime. It is clear that the pulsar was born well below the rebirth line, and the mean accretion rate during the spin-up phase (the final major accretion phase) was lower than 10^{-} $\dot{M}$.

Two groups have run detailed simulations of the evolution of PSR J1614–2230. The Lin et al. (2011) model and the preferred model of Tauris et al. (2011) are qualitatively similar: the system begins as an intermediate mass X-ray binary consisting of a NS and a ~ 4 M$_\odot$ main-sequence secondary, which evolves to form a CO WD with an He envelope. The secondary accretes mass onto the NS in three phases. The first phase (A1) is a thermal timescale mass transfer at super-Eddington accretion rates, where the NS gains little mass. The next phase (A2) is on a nuclear timescale (~ 35 Myr), when the secondary is burning H in the core and envelope. During this phase, the accretion rates are upto about a tenth of the Eddington limit. During the final accretion phase (phase AB), the secondary is burning He in its core and H in an envelope. This causes the radius of the donor star to expand, triggering accretion at near-Eddington rates for 5–10 Myr. The NS gains the most mass during this phase. For typical NS parameters, accreting 0.1–0.2 M$_\odot$ is enough to spin them

up millisecond periods (Kiziltan & Thorsett, 2010). Hence, the near-Eddington accretion in phase AB should spin the pulsar up all the way to the rebirth line. This is inconsistent with our inferred birth position of PSR J1614–2230.

If the stellar evolution models are correct, then there is a problem with the standard formation scenario of MSPs (Radhakrishnan & Srinivasan, 1982; Alpar et al., 1982). In essence, the birth period depends on factors other than the magnetic field strength and accretion rates. For instance, Bildsten (1998, 2003) proposes that accretion induces a quadrupole moment Q in the NS. The NS then loses angular momentum by gravitational wave radiation. Since the magnetic fields do not play any significant role in this model, the rebirth line becomes irrelevant, and PSR J1614–2230 may start its life anywhere on the P–$\dot{P}$ diagram. In summary, the birth of PSR J1614–2230 away from the rebirth line requires reconsideration of angular momentum loss mechanisms.

Going forward, on-going radio observations (pulsar timing and VLBI) should improve the parallax and thereby decrease the uncertainty in the inferred $\dot{P}$ and thus better locate the pulsar in the P-$\dot{P}$ diagram. The scattered light from light Q, while bothersome to the present observations, provide an opportunity to use adaptive optics to measure the near-IR fluxes of the WD. Grism spectroscopy with *Hubble Space Telescope* can potentially reveal the presumed H+He layer posited by stellar evolutionary models of Tauris et al. (2011).

Acknowledgments. We are grateful to Scott Ransom for providing the source position in advance of the publication. We thank M. Kasliwal and A. Gal-Yam for undertaking the observations.

Some of the data presented herein were obtained at the W.M. Keck Observatory, which is operated as a scientific partnership among the California Institute of Technology, the University of California and the National Aeronautics and Space Administration. The Observatory was made possible by the generous financial support of the W.M. Keck Foundation.

Chapter 8

Conclusions and Future Work

When we started the X-Mas survey, masses had been measured for only six neutron stars in high-mass X-ray binaries. To date, we have contributed three of the dozen known masses in this list (Figure 8.1). Our measurements fully support the initial hypothesis that NSs in HMXBs have a wide spread in masses. X-Mas is an ongoing program, and we will add a

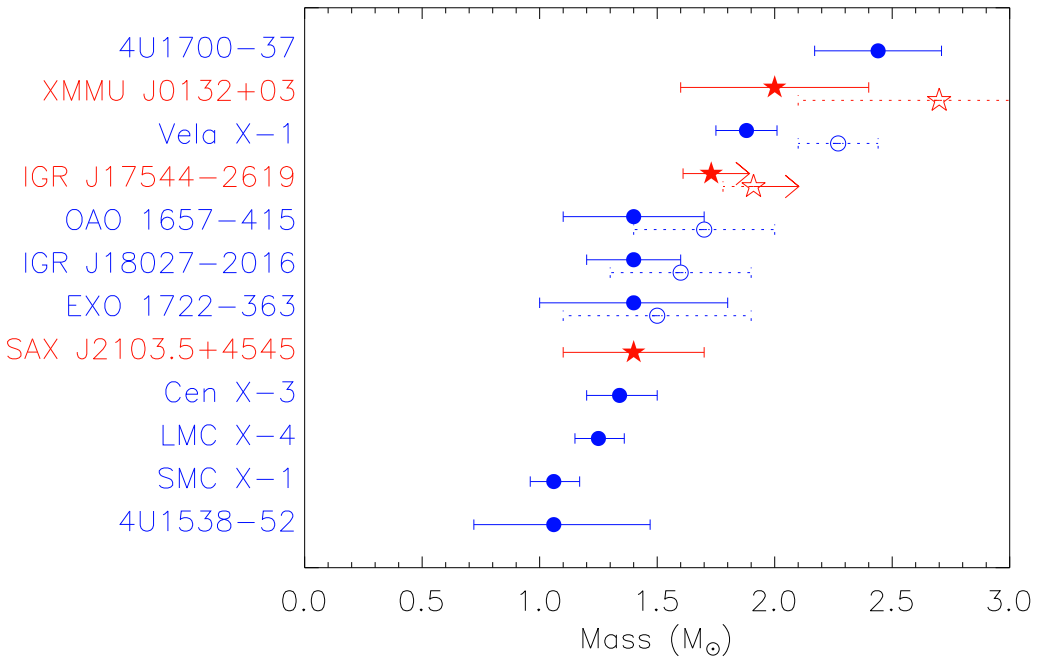

Figure 8.1. All known masses of neutron stars in HMXBs. Red ★ indicate mass measurements discussed in this thesis, blue • are measurements in literature. For Vela X-1, OAO 1654–415, IGR J18027–2016 and EXO1722–363, the solid and hollow symbols correspond edge-on and Roche-filling systems respectively. For references see Table 4.1.

few more measurements to this list.

Neutron star mass measurements have come to a stage where they provide critical feedback to fundamental physics. The recent discovery of a two solar mass neutron star (Demorest et al., 2010) has ruled out some equations of state which preclude the existence of such heavy NSs (Figure 4.1). We can push these limits futher by finding heavier NSs or improving constraints on the existing heavy candidates like 4U 1700−37 (Clark et al., 2002) and XMMU J013236.7+303228 (Chapter 6). For instance, the discovery of a 2.5 $M_\odot$ object can rule out most proposed EOSs, leaving only a few candidates like MS0 and MS2 (Lattimer & Prakash, 2007).

Beyond constraints on the EOS, an intriguing open question is the paucity of compact objects in the 2.5 – 6 solar mass regime (e.g., Remillard & McClintock, 2006; Özel et al., 2010). While all neutron stars have masses $\lesssim 2.5\ M_\odot$, the six stellar-mass black holes with dynamical mass measurements are all heavier than 6 $M_\odot$ (Figure 8.2). This gap in masses of compact objects persists even after accounting for lower limits on masses of other black holes (Özel et al., 2012). While fundamental physics sets the maximum mass for a NS, it does not rule out the formation of, say, a four solar mass black hole. Instead, this gap must arise from the astrophysical scenarios in which black holes form. This gap also suggests the possibility that the distribution of NS masses will probably not have a sharp cutoff governed by fundamental physics. Instead, the formation mechanisms pertaining to core collapse of massive stars do not form compact objects in this regime. More and more robust neutron star mass measurements will enable us to confirm or refute the existence of this gap.

Over the course of this project, we have developed and refined methods for obtaining accurate radial velocity measurements of OB stars. We learned some important lessons along the way, which will help us in planning any future observations. For planning the observing runs, wherever possible, we will choose the spectrograph position angle to place a reference star on the slit along with the target. We can measure the velocity of the target with respect to this star, to overcome systematic errors in data analysis. We will also consider using multi-slit spectrographs for this purpose. In previous observing runs, we obtained calibration arc data at the position of each target. In data analysis we discovered that DBSP and LRIS have very stable wavelength solutions, so we can save time by skipping this step, and obtaining more arc lamp exposures and flat fields at the start

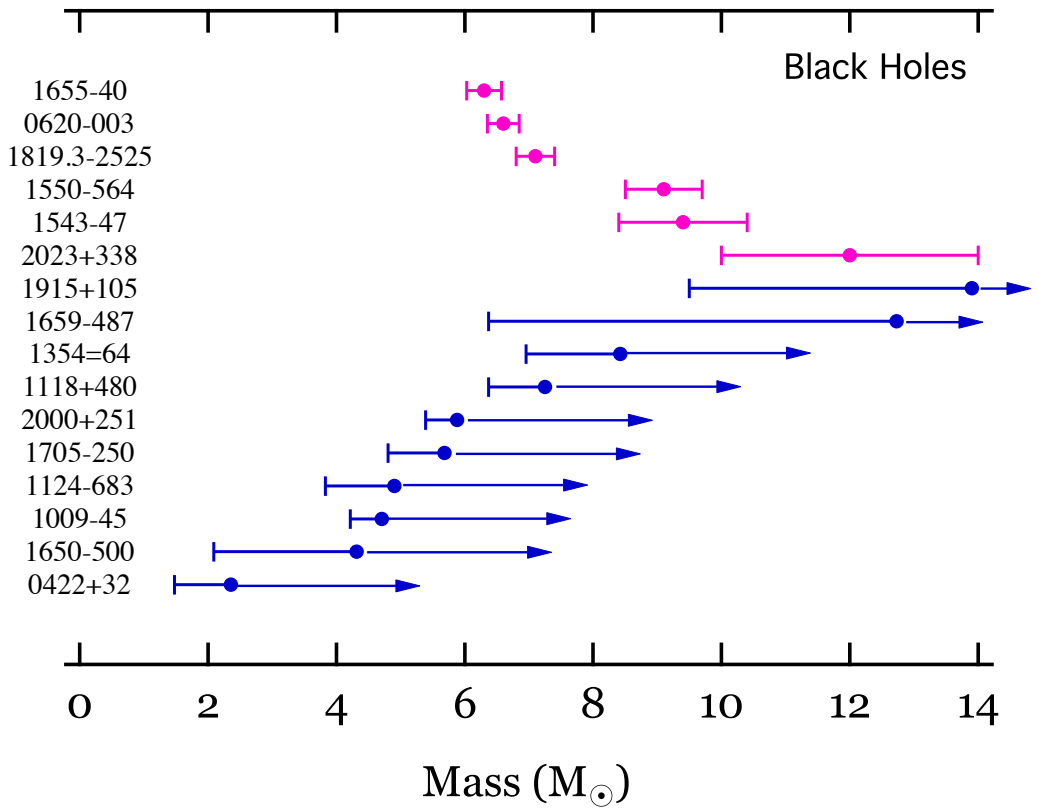

Figure 8.2. Masses of Black Holes: Dynamical measurements have yielded masses for only six stellar mass BHs (magenta data points, top). Lower limits on mass are known for several other systems (blue data points). There are no known compact objects with masses in the range of three to six solar masses. Image reproduced with permission from Özel et al. (2012).

of the night. It was useful to split the total observing time for a target into multiple exposures. In case there were problems like tracking issues or bad readout during any of the exposures, it does not ruin the complete data for that target for that night. We also learned several lessons in data reduction and analysis, which often involved reprocessing data to get better results. I have compiled these in a separate document, available online at http://authors.library.caltech.edu/31417.

This field is in an exciting phase now, with several developments favoring the exploration of NS masses. *Integral* is continuing to finding new X-ray binaries. The upcoming *AstroSat* and NuSTAR missions will enable X-ray timing measurements for many such systems. Beyond X-ray binaries, extensive radio surveys are studying neutron stars for projects like Nanograv. Serendipitously discovered NS binaries in such systems can also be studied to measure NS masses. This ever increasing sample of neutron star masses will help us better understand neutron stars from the context of both: fundamental physics and astrophysics.

Appendix

This is an abridged version of the thesis for file size considerations. Please download the complete version from http://thesis.library.caltech.edu.

Bibliography

Abdo, A. A., Ackermann, M., Ajello, M., Atwood, W. B., Axelsson, M., et al. 2010, The Astrophysical Journal Supplement Series, 187, 460

Agrawal, P. 2006, Advances in Space Research, 38, 2989

Alpar, M. A., Cheng, A. F., Ruderman, M. A., & Shaham, J. 1982, Nature, 300, 728

Arzoumanian, Z., Cordes, J. M., & Wasserman, I. 1999, The Astrophysical Journal, 520, 696

Bailes, M., Bates, S. D., Bhalerao, V., Bhat, N. D. R., Burgay, M., et al. 2011, Science, 1

Barthelmy, S. D., Barbier, L. M., Cummings, J. R., Fenimore, E. E., Gehrels, N., et al. 2005, Space Science Reviews, 120, 143

Barziv, O., Kaper, L., Van Kerkwijk, M. H., Telting, J. H., & Van Paradijs, J. 2001, Astronomy and Astrophysics, 377, 925

Bessell, M. S., Castelli, F., & Plez, B. 1998, Astronomy and Astrophysics, 250, 231

Bhalerao, V. B., & Kulkarni, S. R. 2011, The Astrophysical Journal, 737, L1

Bhalerao, V. B., van Kerkwijk, M. H., Harrison, F. A., Kasliwal, M. M., Kulkarni, S. R., & Rana, V. R. 2010, The Astrophysical Journal, 721, 412

Bhattacharya, D., & van den Heuvel, E. P. J. 1991, Physics Reports, 203, 1

Bildsten, L. 1998, The Astrophysical Journal, 501, L89

—. 2003, Radio Pulsars, 302

Blackburn, J. K. 1995, Astronomical Data Analysis Software and Systems IV, 77

Bolotnikov, A., Cook, W., Harrison, F., Wong, A.-S., Schindler, S., & Eichelberger, A. 1999, Nuclear Instruments and Methods in Physics Research Section A: Accelerators, Spectrometers, Detectors and Associated Equipment, 432, 326

Bonnet-Bidaud, J. M., & Mouchet, M. 1998, Astronomy and Astrophysics, 12, 9

Bonsema, P. F. J., & van den Heuvel, E. P. J. 1985, Astronomy and Astrophysics, 146

Brott, I., de Mink, S. E., Cantiello, M., Langer, N., de Koter, A., et al. 2011, Astronomy & Astrophysics, 530, A115

Camero Arranz, A., Wilson, C. A., Finger, M. H., & Reglero, V. 2007, Astronomy and Astrophysics, 473, 551

Camilo, F., Thorsett, S. E., & Kulkarni, S. R. 1994, The Astrophysical Journal, 421, L15

Casares, J., Hernández, J. I. G., Israelian, G., & Rebolo, R. 2010, Monthly Notices of the Royal Astronomical Society, 401, 2517

Cenko, S. B., Fox, D. B., Moon, D., Harrison, F. A., Kulkarni, S. R., et al. 2006, Publications of the Astronomical Society of the Pacific, 118, 1396

Chabrier, G., Brassard, P., Fontaine, G., & Saumon, D. 2000, The Astrophysical Journal, 543, 216

Chaty, S. 2011, Evolution of compact binaries. Proceedings of a workshop held at Hotel San Martín, 447

Chaty, S., Zurita Heras, J. A., & Bodaghee, A. 2010, eprint arXiv:1012.2318

Christensen, F. E., Hornstrup, A., Westergaard, N. J., Schnopper, H. W., Wood, J., & Parker, K. 1992, In: Multilayer and grazing incidence X-ray/EUV optics; Proceedings of the Meeting, 160

Christensen, F. E., Jakobsen, A. C., Brejnholt, N. F., Madsen, K. K., Hornstrup, A., et al. 2011, in Society of Photo-Optical Instrumentation Engineers (SPIE) Conference Series, Vol. 8147, 81470U–81470U–19

Clark, D. J., Hill, A. B., Bird, A. J., McBride, V. A., Scaringi, S., & Dean, A. J. 2009, Monthly Notices of the Royal Astronomical Society: Letters, 399, L113

Clark, J. S., Goodwin, S. P., Crowther, P. A., Kaper, L., Fairbairn, M., Langer, N., & Brocksopp, C. 2002, Astronomy and Astrophysics, 392, 909

Cordes, J. M., & Lazio, T. J. W. 2002, eprint arXiv:astro-ph/0207156

Cox, A. N. 2000, Allen's astrophysical quantities

Cropper, M. 1990, Space Science Reviews, 54, 195

de Vaucouleurs, G., de Vaucouleurs, A., Corwin, Herold G., J., Buta, R. J., Paturel, G., & Fouque, P. 1991, Volume 1-3, 1

Deloye, C. J., & Bildsten, L. 2003, The Astrophysical Journal, 598, 1217

Demorest, P. B., Pennucci, T., Ransom, S. M., Roberts, M. S. E., & Hessels, J. W. T. 2010, Nature, 467, 1081

Denisenko, D. V., Kryachko, T. V., & Satovskiy, B. L. 2009, The Astronomer's Telegram

Drave, S. P., Bird, A. J., Townsend, L. J., Hill, A. B., McBride, V. A., Sguera, V., Bazzano, A., & Clark, D. J. 2012, Astronomy & Astrophysics, 539, A21

Edwards, R., Bailes, M., van Straten, W., & Britton, M. 2001, Monthly Notices of the Royal Astronomical Society, 326, 358

Eggleton, P. P. 1983, The Astrophysical Journal, 268, 368

Figueira, P., Pepe, F., Lovis, C., & Mayor, M. 2010, Astronomy and Astrophysics, 515, A106

Frank, J., King, A. R., & Raine, D. J. 1985, Accretion power in astrophysics

Freedman, W. L., Madore, B. F., Gibson, B. K., Ferrarese, L., Kelson, D. D., et al. 2001, The Astrophysical Journal, 553, 47

Freire, P. C. C., Ransom, S. M., Bégin, S., Stairs, I. H., Hessels, J. W. T., Frey, L. H., & Camilo, F. 2008, The Astrophysical Journal, 675, 670

Fruchter, A. S., Stinebring, D. R., & Taylor, J. H. 1988, Nature, 333, 237

Galloway, D. K., Chakrabarty, D., Morgan, E. H., & Remillard, R. A. 2002, The Astrophysical Journal, 576, L137

Gehrels, N., Chincarini, G., Giommi, P., Mason, K. O., Nousek, J. A., et al. 2004, The Astrophysical Journal, 611, 1005

Giacconi, R., Gursky, H., Paolini, F., & Rossi, B. 1962, Physical Review Letters, 9, 439

Giacconi, R., Branduardi, G., Briel, U., Epstein, A., Fabricant, D., et al. 1979, The Astrophysical Journal, 230, 540

Gray, D. F. 2005, The Observation and Analysis of Stellar Photospheres

Grindlay, J. E., & Bailyn, C. D. 1988, Nature, 336, 48

Hailey, C. J., An, H., Blaedel, K. L., Brejnholt, N. F., Christensen, F. E., et al. 2010, in Space Telescopes and Instrumentation 2010: Ultraviolet to Gamma Ray. Edited by Arnaud, Vol. 7732, 77320T–77320T–13

Hansen, B. M. S., Shih, H.-Y., & Currie, T. 2009, The Astrophysical Journal, 691, 382

Harrison, F. A., Christensen, F. E., Craig, W., Hailey, C., Baumgartner, W., et al. 2006, Experimental Astronomy, 20, 131

Harrison, F. A., Boggs, S., Christensen, F., Craig, W., Hailey, C., et al. 2010, in Space Telescopes and Instrumentation 2010: Ultraviolet to Gamma Ray. Edited by Arnaud, Vol. 7732, 77320S–77320S–8

Harrison, M., McGregor, D., & Doty, F. 2008, Physical Review B, 77

Harwit, M. 2003, Physics Today, 56, 38

Hellier, C. 2001, Cataclysmic Variable Stars

—. 2002, The Physics of Cataclysmic Variables and Related Objects, 261

Hessels, J., Ransom, S., Roberts, M., Kaspi, V., Livingstone, M., Tam, C., & Crawford, F. 2005, Binary Radio Pulsars, 328

Hessels, J. W. T., Ransom, S. M., Stairs, I. H., Freire, P. C. C., Kaspi, V. M., & Camilo, F. 2006, Science (New York, N.Y.), 311, 1901

Hilditch, R. W. 2001, An Introduction to Close Binary Stars, 1st edn. (Cambridge, UK: Cambridge University Press)

Hilditch, R. W., Howarth, I. D., & Harries, T. J. 2005, Monthly Notices of the Royal Astronomical Society, 357, 304

Hulleman, F., in 't Zand, J. J. M., & Heise, J. 1998, Astronomy and Astrophysics, 337, L25

in 't Zand, J. J. M. 2005, Astronomy and Astrophysics, 441, L1

Iniewski, K. 2010, Semiconductor radiation detection systems (Boca Raton FL: CRC Press/Taylor & Francis)

Jacoby, B. A., Hotan, A., Bailes, M., Ord, S., & Kulkarni, S. R. 2005, The Astrophysical Journal, 629, L113

Jahoda, K., Swank, J. H., Giles, A. B., Stark, M. J., Strohmayer, T., Zhang, W., & Morgan, E. H. 1996, Proc. SPIE Vol. 2808, 2808, 59

Jester, S., Schneider, D. P., Richards, G. T., Green, R. F., Schmidt, M., et al. 2005, The Astronomical Journal, 130, 873

Joss, P. C., & Rappaport, S. A. 1984, Annual Review of Astronomy and Astrophysics, 22, 537

Juett, A. M., Psaltis, D., & Chakrabarty, D. 2001, The Astrophysical Journal, 560, L59

Kaspi, V. M., Lyne, A. G., Manchester, R. N., Crawford, F., Camilo, F., et al. 2000, The Astrophysical Journal, 543, 321

Kaur, R., Wijnands, R., Paul, B., Patruno, A., & Degenaar, N. 2010, Monthly Notices of the Royal Astronomical Society, 402, 2388

Keith, M. J., Jameson, A., Van Straten, W., Bailes, M., Johnston, S., et al. 2010, Monthly Notices of the Royal Astronomical Society, 409, 619

Keith, M. J., Johnston, S., Ray, P. S., Ferrara, E. C., Saz Parkinson, P. M., et al. 2011, Monthly Notices of the Royal Astronomical Society, 414, 1292

Kiziltan, B., Kottas, A., & Thorsett, S. E. 2010, eprint arXiv:1011.4291

Kiziltan, B., & Thorsett, S. E. 2010, The Astrophysical Journal, 715, 335

Knigge, C., Coe, M. J., & Podsiadlowski, P. 2011, Nature, 479, 372

Kolb, U., King, A. R., & Baraffe, I. 2001, Monthly Notices of the Royal Astronomical Society, 321, 544

Kzlolu, U., Kzlolu, N., Baykal, A., Yerli, S. K., & Özbey, M. 2007, Astronomy and Astrophysics, 470, 1023

Lai, D., Abrahams, A. M., & Shapiro, S. L. 1991, The Astrophysical Journal, 377, 612

Landsman, W. B. 1993, Astronomical Data Analysis Software and Systems II, 52

Lang, D., Hogg, D. W., Mierle, K., Blanton, M., & Roweis, S. 2010, The Astronomical Journal, 139, 1782

Lattimer, J., & Prakash, M. 2005, Physical Review Letters, 94

Lattimer, J. M., & Prakash, M. 2004, Science (New York, N.Y.), 304, 536

—. 2007, Physics Reports, 442, 109

Lattimer, J. M., Prakash, M., Day, R. R., & Year, M. 2010, eprint arXiv:1012.3208, 1

Law, N. M., Kulkarni, S. R., Dekany, R. G., Ofek, E. O., Quimby, R. M., et al. 2009, Publications of the Astronomical Society of the Pacific, 121, 1395

Lebrun, F., Leray, J. P., Lavocat, P., Crtolle, J., Arqus, M., et al. 2003, Astronomy and Astrophysics, 411, L141

Lin, J., Rappaport, S., Podsiadlowski, P., Nelson, L., Paxton, B., & Todorov, P. 2011, The Astrophysical Journal, 732, 70

Liu, Q. Z., van Paradijs, J., & van den Heuvel, E. P. J. 2005, Astronomy and Astrophysics, 442, 1135

—. 2006, Astronomy and Astrophysics, 455, 1165

Longair, M. S. 1992, High Energy Astrophysics

Madsen, K. K., Harrison, F. a., Mao, P. H., Christensen, F. E., Jensen, C. P., Brejnholt, N., Koglin, J., & Pivovaroff, M. J. 2009, Proceedings of SPIE, 7437, 743716

Manchester, R. N., Hobbs, G. B., Teoh, A., & Hobbs, M. 2005, The Astronomical Journal, 129, 1993

Mao, P. H., Harrison, F. A., Windt, D. L., & Christensen, F. E. 1999, Applied Optics, 38, 4766

Markwardt, C. B. 2009, Astronomical Data Analysis Software and Systems XVIII ASP Conference Series, 411

Mason, A. B., Clark, J. S., Norton, A. J., Crowther, P. A., Tauris, T. M., Langer, N., Negueruela, I., & Roche, P. 2011a, Monthly Notices of the Royal Astronomical Society, 000, 10

Mason, A. B., Norton, A. J., Clark, J. S., Negueruela, I., & Roche, P. 2011b, Astronomy & Astrophysics, 532, A124

Mason, A. B., Norton, A. J., Clark, J. S., Roche, P., & Negueruela, I. 2010, Société Royale des Sciences de Liège, 80, 699

Massey, P., Morrell, N. I., Neugent, K. F., Penny, L. R., Eastwood, K.-D., & Gies, D. R. 2012, Physics

McCarthy, J. K., Cohen, J. G., Butcher, B., Cromer, J., Croner, E., et al. 1998, Proc. SPIE Vol. 3355, 3355, 81

McConnachie, A. W., Irwin, M. J., Ferguson, A. M. N., Ibata, R. A., Lewis, G. F., & Tanvir, N. 2005, Monthly Notices of the Royal Astronomical Society, 356, 979

McLean, I. S., McGovern, M. R., Burgasser, A. J., Kirkpatrick, J. D., Prato, L., & Kim, S. S. 2003, The Astrophysical Journal, 596, 561

McLean, I. S., Becklin, E. E., Bendiksen, O., Brims, G., Canfield, J., et al. 1998, Proc. SPIE Vol. 3354, 3354, 566

Mighell, K. J. 1999, Astronomical Data Analysis Software and Systems VIII, 172

Munari, U., Sordo, R., Castelli, F., & Zwitter, T. 2005, Astronomy and Astrophysics, 442, 1127

MunozDarias, T., Casares, J., & MartinezPais, I. G. 2005, The Astrophysical Journal, 635, 502

Negueruela, I., & Schurch, M. P. E. 2007, Astronomy and Astrophysics, 461, 631

Niemela, A., & Sipila, H. 1994, IEEE Transactions on Nuclear Science, 41, 1054

Nomoto, K. 1984, The Astrophysical Journal, 277, 791

Oke, J. B., & Gunn, J. E. 1982, Publications of the Astronomical Society of the Pacific, 94, 586

Oke, J. B., Cohen, J. G., Carr, M., Cromer, J., Dingizian, A., et al. 1995, Publications of the Astronomical Society of the Pacific, 107, 375

Özel, F., Psaltis, D., Narayan, R., & McClintock, J. E. 2010, The Astrophysical Journal, 725, 1918

Özel, F., Psaltis, D., Narayan, R., & Villarreal, A. S. 2012, arXiv eprint

Paczynski, B. 1971, Annual Review of Astronomy and Astrophysics, 9, 183

Paul, B., & Naik, S. 2011, Bulletin of the Astronomical Society of India, 39, 429

Pellizza, L. J., Chaty, S., & Negueruela, I. 2006, Astronomy and Astrophysics, 455, 653

Pietsch, W., Misanovic, Z., Haberl, F., Hatzidimitriou, D., Ehle, M., & Trinchieri, G. 2004, Astronomy and Astrophysics, 426, 11

Pietsch, W., Plucinsky, P. P., Haberl, F., Shporer, A., & Mazeh, T. 2006, The Astronomer's Telegram, 905, 1

Pietsch, W., Haberl, F., Gaetz, T. J., Hartman, J. D., Plucinsky, P. P., et al. 2009, The Astrophysical Journal, 694, 449

Podsiadlowski, P. 1993, in Planets around pulsars; Proceedings of the Conference, ed. J. A. Phillips, S. E. Thorsett, & S. R. Kulkarni, Vol. 36, 149–165

Poole, T. S., Breeveld, A. A., Page, M. J., Landsman, W., Holland, S. T., et al. 2007, Monthly Notices of the Royal Astronomical Society, 383, 627

Quaintrell, H., Norton, A. J., Ash, T. D. C., Roche, P., Willems, B., Bedding, T. R., Baldry, I. K., & Fender, R. P. 2003, Astronomy and Astrophysics, 401, 313

Radhakrishnan, V., & Srinivasan, G. 1982, Current Science, 51, 1096

Rahoui, F., Chaty, S., Lagage, P.-O., & Pantin, E. 2008, Astronomy and Astrophysics, 484, 801

Ramsay, G., Cropper, M., Wu, K., Mason, K. O., Córdova, F. A., & Priedhorsky, W. 2004, Monthly Notices of the Royal Astronomical Society, 350, 1373

Rappaport, S., Podsiadlowski, P., Joss, P. C., Di Stefano, R., & Han, Z. 1995, Monthly Notices of the Royal Astronomical Society, 273, 731

Rappaport, S. A., & Joss, P. C. 1983, IN: Accretion-driven stellar X-ray sources (A84-35577 16-90). Cambridge and New York, 1

Rasio, F. A., Shapiro, S. L., & Teukolsky, S. A. 1992, Astronomy and Astrophysics (ISSN 0004-6361), 256

Reig, P. 2011, Astrophysics and Space Science, 332, 1

Reig, P., Negueruela, I., Fabregat, J., Chato, R., Blay, P., & Mavromatakis, F. 2004, Astronomy and Astrophysics, 421, 673

Remillard, R. A., & McClintock, J. E. 2006, Annual Review of Astronomy and Astrophysics, 44, 49

Rephaeli, Y., Nevalainen, J., Ohashi, T., & Bykov, A. M. 2008, Space Science Reviews, 134, 71

Roberts, M. S. E., Gotthelf, E. V., Halpern, J. P., Brogan, C. L., & Ransom, S. M. 2007, Proceedings of the 363. WE-Heraeus Seminar on Neutron Stars and Pulsars 40 years after the discovery. Edited by W. Becker and H. H. Huang. MPE-Report 291. ISSN 0178-0719. Published by the Max Planck Institut für extraterrestrische Physik

Rockosi, C., Stover, R., Kibrick, R., Lockwood, C., Peck, M., et al. 2010, in Ground-based and Airborne Instrumentation for Astronomy III. Edited by McLean, Vol. 7735, 77350R–77350R–11

Schlegel, D. J., Finkbeiner, D. P., & Davis, M. 1998, The Astrophysical Journal, 500, 525

Schwab, J., Podsiadlowski, P., & Rappaport, S. 2010, The Astrophysical Journal, 719, 722

Shevchuk, A. S., Fox, D. B., Turner, M., & Rutledge, R. E. 2009, The Astronomer's Telegram

Shklovskii, I. S. 1970, Soviet Astronomy, 13

Shporer, A., Hartman, J., Mazeh, T., & Pietsch, W. 2006, The Astronomer's Telegram, 913, 1

Sidoli, L. 2011, Advances in Space Research, 48, 88

Simcoe, R. A., Metzger, M. R., Small, T. A., & Araya, G. 2000, American Astronomical Society, 32

Smith, D. M. 2004, The Astronomer's Telegram

Stappers, B. W., Bailes, M., Manchester, R. N., Sandhu, J. S., & Toscano, M. 1998, The Astrophysical Journal, 499, L183

Stappers, B. W., van Kerkwijk, M. H., Lane, B., & Kulkarni, S. R. 1999, The Astrophysical Journal, 510, L45

Steidel, C. C., Shapley, A. E., Pettini, M., Adelberger, K. L., Erb, D. K., Reddy, N. A., & Hunt, M. P. 2004, The Astrophysical Journal, 604, 534

Steiner, A. W., Lattimer, J. M., & Brown, E. F. 2010, The Astrophysical Journal, 722, 33

Sunyaev, R. A., Grebenev, S. A., Lutovinov, A. A., Rodriguez, J., Mereghetti, S., Gotz, D., & Courvoisier, T. 2003, The Astronomer's Telegram, 190, 1

Takahashi, T., Abe, K., Endo, M., Endo, Y., Ezoe, Y., et al. 2007, Publications of the Astronomical Society of Japan

Tauris, T. M., Langer, N., & Kramer, M. 2011, Monthly Notices of the Royal Astronomical Society, 416, 2130

Timmes, F. X., Woosley, S. E., & Weaver, T. A. 1996, The Astrophysical Journal, 457, 834

Torres, G. 2010, The Astronomical Journal, 140, 1158

Toscano, M., Sandhu, J. S., Bailes, M., Manchester, R. N., Britton, M. C., Kulkarni, S. R., Anderson, S. B., & Stappers, B. W. 1999, Monthly Notices of the Royal Astronomical Society, 307, 925

Tousey, R., Watanabe, K., & Purcell, J. 1951, Physical Review, 83, 792

Ubertini, P., Lebrun, F., Di Cocco, G., Bazzano, A., Bird, A. J., et al. 2003, Astronomy and Astrophysics, 411, L131

Valentim, R., Rangel, E., & Horvath, J. E. 2011, Monthly Notices of the Royal Astronomical Society, 414, 1427

van den Heuvel, E. P. J., & Bonsdema, P. T. J. 1984, Astronomy and Astrophysics (ISSN 0004-6361), 139

van der Meer, A., Kaper, L., van Kerkwijk, M. H., Heemskerk, M. H. M., & van den Heuvel, E. P. J. 2007, Astronomy and Astrophysics, 473, 523

van Dokkum, P. G. 2001, Publications of the Astronomical Society of the Pacific, 113, 1420

van Kerkwijk, M. H., Breton, R. P., & Kulkarni, S. R. 2011, The Astrophysical Journal, 728, 95

van Kerkwijk, M. H., van Paradijs, J., Zuiderwijk, E. J., Hammerschlag-Hensberge, G., Kaper, L., & Sterken, C. 1995, Astronomy and Astrophysics

Verbiest, J. P. W., Bailes, M., van Straten, W., Hobbs, G. B., Edwards, R. T., et al. 2008, The Astrophysical Journal, 679, 675

Voges, W., Aschenbach, B., Boller, T., Bräuninger, H., Briel, U., et al. 1999, Astronomy and Astrophysics

Walborn, N. R., & Fitzpatrick, E. L. 1990, Publications of the Astronomical Society of the Pacific, 102, 379

Warner, B. 1995, Camb. Astrophys. Ser., 28

Weisskopf, M. C., Tananbaum, H. D., Van Speybroeck, L. P., & O'Dell, S. L. 2000, Proc. SPIE Vol. 4012, 4012, 2

Wijers, R. A. M. J., van den Heuvel, E. P. J., van Kerkwijk, M. H., & Bhattacharya, D. 1992, Nature, 355, 593

Wilson, C. A., Finger, M. H., Harmon, B. A., Chakrabarty, D., & Strohmayer, T. 1998, The Astrophysical Journal, 499, 820

Wilson, C. A., Weisskopf, M. C., Finger, M. H., Coe, M. J., Greiner, J., Reig, P., & Papamastorakis, G. 2005, The Astrophysical Journal, 622, 1024

Wolszczan, A., & Frail, D. A. 1992, Nature, 355, 145

Wolter, H. 1952a, Annalen der Physik, 445, 286

—. 1952b, Annalen der Physik, 445, 94

York, D. G., Adelman, J., Anderson, J., Anderson, S. F., Annis, J., et al. 2000, The Astronomical Journal, 120, 1579

Zhang, C. M., Wang, J., Zhao, Y. H., Yin, H. X., Song, L. M., et al. 2011, Astronomy & Astrophysics, 527, A83

Zwitter, T., Castelli, F., & Munari, U. 2004, Astronomy and Astrophysics, 417, 1055